Modelling the Composition-Dependent Anisotropy of Ultra-High-Energy Cosmic Rays Through Propagation in the Galactic Magnetic Field

Master's Thesis in Physics

Presented by
Chaimongkol Duangchan
August 24, 2023

Erlangen Centre for Astroparticle Physics
Friedrich-Alexander-Universität Erlangen-Nürnberg

Supervisor: Prof. Dr. Stefan Funk

Abstract

The origin of ultra-high-energy cosmic rays (UHECRs) has been an open question for over half a century. The Pierre Auger Observatory is one of the ground-based cosmic ray detectors capable of observing in the ultra-high-energy range. Reports from the collaboration found composition-dependent anisotropy, where the heavier composition is more populated in the direction along the galactic plane, whereas the lighter composition is more populated towards the galactic pole. This gives a clue to understanding the source of these cosmic particles at extreme energy. It is also suggested that this phenomenon arises from the deflection by the galactic magnetic field.

In this thesis, a simulation method for constructing the composition sky map is introduced to test the statement. The initial investigation focuses on understanding the influence of the galactic magnetic field on the deflection of extragalactic UHECR. This analysis relies on simulating the propagation of UHECRs in the galactic magnetic field using the lensing technique. The study assumes an isotropic source distribution. The outcome unveils a smoother flux distribution characterized by the width of the arrival flux distribution, which is observed to be dependent on rigidity.

Next, to create the composition-dependent distribution, the simulated events are drawn using the propagated flux map as a probability basis. A cut-off power law is assumed for equal injection of both proton and iron nuclei. This provides spatial and spectral distribution of the events. The mass observables are assigned to the simulated data set using the distribution fitted to the simulation of air showers. The results indicate that the galactic magnetic field does not solely account for the composition anisotropy. Additionally, another source distribution hypothesis is analyzed and presented, further supporting the conclusions of this work.

Keywords: Ultra-high energy cosmic ray, Galactic propagation, Magnetic lensing

Contents

1 Introduction **6**

2 Detection of UHECR **8**
2.1 Properties of Air Showers 8
2.1.1 Longitudinal profile 9
2.1.2 Lateral Profile 10
2.2 The Pierre Auger Observatory 11
2.2.1 The infrastructure 11
2.2.2 Direction reconstruction 14
2.2.3 Longitudinal profile reconstruction 15
2.2.4 Energy reconstruction 16
2.3 Highlighted discoveries 17
2.3.1 UHECR spectrum above 2.5 EeV 17
2.3.2 Energy dependence in UHECR penetration 18
2.3.3 Dipolar distribution of UHECR flux above 8 EeV 19
2.3.4 UHECR composition anisotropy found above 5 EeV 20

3 Propagation of UHECR in the Galactic Magnetic Field **21**
3.1 Galactic magnetic field model 21
3.2 Magnetic lensing 24
3.2.1 Production of the magnetic lens 24
3.2.2 Forward propagation using magnetic lens 26
3.3 Propagation of the isotropic source distribution 27
3.3.1 Magnetic field effectiveness 28
3.3.2 Arrival probability as a function of galactic latitude 31
3.4 Simulation of detection at Earth 36
3.4.1 Average flux as a function of galactic latitude 36
3.4.2 Angular power spectrum 38

4 Mass Anisotropy Analysis **42**
4.1 The mass observable distribution 42
4.2 Simulated observations 44
4.3 The composition map 46
4.4 Selected scenarios 49
4.4.1 Variation in relative component 49
4.4.2 Dipolar distribution 49

5 Conclusion and Outlook **52**

A Energy loss due to magnetic field **53**

B Arrival probability over galactic latitude **54**

C Effectiveness parameter for different number of initial particles **58**

D Description of the generalized Gumbel distribution **62**
D.1 Parametrization 62
D.2 Transformation of shape parameter 63

Bibliography **67**

Acknowledgement **68**

Chapter 1

Introduction

The study of cosmic radiation initially became known through the remarkable work of Victor Franz Hess in 1912 [1], although the term 'cosmic ray' was given a decade later by another Nobel laureate, Robert Andrews Millikan [2]. At that time, there were still controversies about the source accounting for the high-energy radiation, but the results from Victor Hess's balloon experiment—which later awarded him the Nobel Prize—resolved this open question. By conducting numerous balloon flights measuring radiation at various altitudes up to approximately 5 km, the increase in radiation intensity found in his results was against the ground-level source hypothesis: this could be a result originating from outer space. Currently, we know that his measurement is a trace of 'air showers' originating from the cosmic ray.

Since the discovery in the early 20th century, and with the technological advancements in cosmic ray observatories, we are now able to achieve the measurements of ultra-high-energy cosmic rays (UHECRs) [3, 4]. The term ultra-high energy (UHE) refers to energy ranging from 10^{18} eV, while the current accelerator, e.g. the Large Hardon Collider (LHC), only archives 5 orders of magnitude lower [5]. However, the integrated flux of UHECR is exceptionally rare with an average detection rate of a single event per square kilometer per year. Therefore, The Pierre Auger Observatory, the current largest UHECR in Argentina, is built to measure this tiny fraction in the cosmic ray spectrum. It detects the signals from secondary particles in the extensive air shower (EAS) produced by UHECR primaries. The measurements are then analyzed to retrieve informationsuch as the energy, arrival direction, and shower geometry of each event. In Chapter 2, the Pierre Auger Observatory is briefly introduced, together with the crucial result and analysis made by the collaborators.

The origin of these extremely high-energy particles remains a mystery. Searching for the sources may be done, for example, by directly comparing the observed arrival distribution to the possible candidates. Another approach is to model the source profile and analyze the related observables. Interestingly, the results announced by the Pierre Auger Collaboration, reveal a dipolar distribution in the measured UHECR flux [6]. This supports the hypothesis that UHECRs have an extragalactic origin, together with the anisotropic distribution of their composition [7].

Considering the situation where some extragalactic cosmic rays (EGCRs) may enter our galaxy's vicinity, if these particles reach Earth, they will propagate through the interstellar medium and the galactic magnetic field (GMF). This environment can

alter their paths and redistribute their arrival distribution measured on Earth.

The primary objective of this thesis is to investigate the influence of the GMF on the arrival composition distribution of UHECR. Since we need to model things that are not directly indicated; therefore, it is beneficial to use simulations. However, the traditional method is not effective in the computational cost, so the alternative method will be discussed. This methodology will be elaborated in Chapter 3, together with the simulation process. Subsequently, the composition anisotropy analysis is shown in Chapter 4 to indicate how strong the GMF influences under the source-independent situation. Finally, the conclusion is in Chapter 5.

Chapter 2

Detection of UHECR

Since the UHECR flux is very subtle, we cannot directly detect UHECRs using typical particle detection techniques. For most ground-based cosmic ray experiments, the atmosphere plays an important role in the detection. When a cosmic ray arriving at Earth hits the atmosphere, it produces numerous daughter particles, or extensive air showers (EAS), from continuous interactions, covering a huge area on the ground. Information on the arriving particle, e.g. arrival direction, and energy, is then retrieved through the detection of the particles from the EAS.

In this chapter, the physics of the creation of EAS, including the interaction model, is explained in summary. Then, the design and detection strategy of the largest UHECR observatory is given, followed by the measurements that motivate this thesis.

2.1 Properties of Air Showers

A cosmic ray air shower refers to the cascade of secondary particles that are created when a high-energy cosmic ray particle interacts with the Earth's atmosphere. These cosmic rays, typically protons or atomic nuclei, may originate from extreme astrophysical objects [8]; they can accelerate particles to reach energies far beyond what can be produced by human-made particle accelerators. As they are spending their time within the colossal accelerators in space, they can acquire energies exceeding 10^{20} eV.

When cosmic rays enter the Earth's atmosphere, they interact and inject their energies, creating numerous amounts of still-high-energy offspring. These daughter nuclei and their descendants will then be produced until the energy drops below the threshold and becomes inactive, similar to the chain reaction in nuclear fission. The description of hadronic interaction in the UHE region is derived using theoretical particle physics, together with the calibration from the collider experiments, e.g. LHC.

The development of a cosmic ray air shower can be divided into two main components: the electromagnetic cascade and the hadronic cascade. The electromagnetic cascade is primarily driven by the production and subsequent interactions of high-energy photons and electrons. These particles generate more photons through

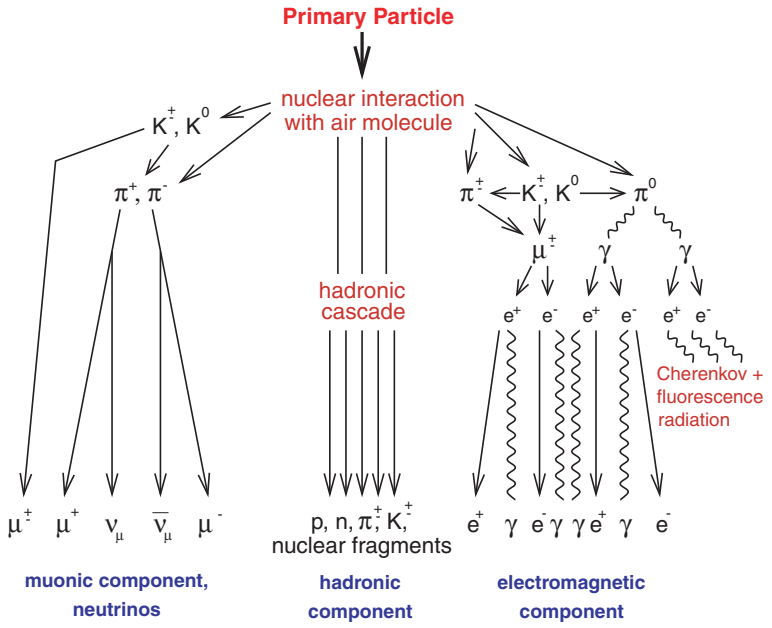

Figure 2.1: Components in the EAS (extracted from [9]).

bremsstrahlung and produce electron-positron pairs via pair production. The hadronic cascade, on the other hand, involves the interactions of high-energy hadrons, such as protons and neutrons, which produce pions and other hadrons. As the air shower progresses, the particles continue to lose energy through ionization, radiation, and other processes. Furthermore, some short-lived hadrons decay into photons creating sub-electromagnetic showers, as shown in Figure 2.1.

Concurrently, another component of the air shower, known as the muonic cascade, occurs. Muons, being relatively more penetrating particles, can travel at considerable distances in the atmosphere without experiencing significant energy loss and eventually reach the ground.

Importantly, we define the atmospheric depth X from the integral of atmospheric density profile $\rho(h)$

$$X(H) = \int_{H}^{\infty} \rho(h)\, dh \tag{2.1}$$

as the distance or the thickness of the atmosphere that the particle has traversed. This also depends on the zenith angle, as particles 'see' a thicker atmosphere for a flat angle. To do so, a factor of $\dfrac{1}{\cos(\theta)}$ is added.

2.1.1 Longitudinal profile

The simplified electromagnetic shower development model was first introduced by Heitler [10] where the interaction length λ_l is assumed to be equal for those lepton pair and photon. It is initiated by a pair-production of a photon shown in Figure 2.2, followed by many fragmentations, either bremsstrahlung of leptons or pair-production of photons. After n successions, the initial energy E_0 is distributed to 2^n particles and reaches the critical energy E_c. Thus, $n = \log_2(E_0/E_c)$. The maximum

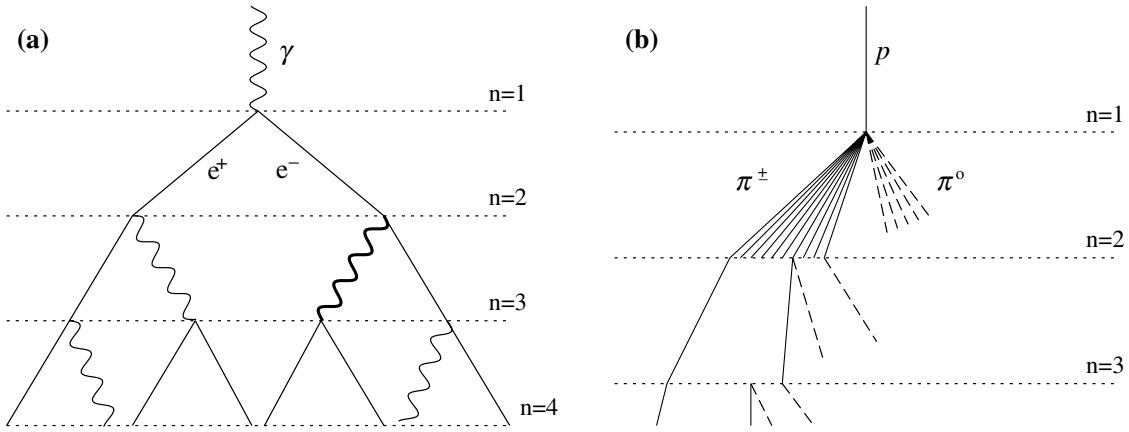

Figure 2.2: Toy model for the Development of (a) electromagnetic shower and (b) hadronic shower (extracted from [11]).

depth $X_{\max}$ is found by n times doubling length $d = \lambda_l \ln 2$, or

$$X_{\max} = \lambda_l \ln \frac{E_0}{E_c}. \tag{2.2}$$

In experiments, it is observed that the branching is not in two-body splitting, so this model might not well-suited. In general, especially for more complex situations, e.g. hadronic interaction, the number of charged particles at each atmospheric depth can usually be fitted to the parametric function introduced by Gaisser and Hillas [12]:

$$N^i(X) = N^i_{\max} \left(\frac{X - X_0}{X^i_{\max} - X_0} \right)^{\frac{X^i_{\max} - X_0}{\lambda^i}} \exp\left(\frac{X^i_{\max} - X}{\lambda^i} \right) \tag{2.3}$$

where i denotes the particle type, the first interaction depth X^i_0, the depth at which the particles are created the most $X^i_{\max}$, and the attenuation depth λ^i varies for each particle i. These parameters relate to the primary and the energy of the incoming cosmic rays.

2.1.2 Lateral Profile

Lateral profile or Lateral Distribution Function (LDF) refers to the spatial distribution of particle densities in the air shower as a function of radial distance from the shower axis. The LDF is typically measured by deploying an array of particle detectors on the ground. These detectors sample the particles within the air shower and record their signals while trespassing. It carries valuable information about the characteristics of the primary cosmic ray, the energy of the shower, and the properties of the interaction between the cosmic ray and the atmosphere. It can also be used to infer the primary cosmic ray's arrival direction, which is determined by the asymmetry in the lateral distribution.

Various mathematical models and empirical parameterizations such as Nishimura-

Kamata-Greisen (NKG) function [13, 14],

$$\rho(r) = \rho_0 \left(\frac{r}{r_c}\right)^{\alpha} \left(1 + \frac{r}{r_c}\right)^{\beta}, \tag{2.4}$$

have been proposed to describe the LDF in extensive air showers. These models take into account factors such as the energy of the primary cosmic ray, the type of the primary particle, and the atmospheric conditions. The fit parameters in these models are determined by comparing the model predictions with experimental data obtained from extensive air shower measurements. For example, regarding Equation 2.4, an electron shower could have:

- r_c as the Molière radius, the shower cross-section radius where most of the energy in the shower has been dissipated;
- $\alpha = s - 2$ where s denotes the shower age parameter;
- $\beta = s - 9/2$;
- $\rho_0 = N_e/2\pi r_c^2 \cdot \Gamma(-\beta)/\Gamma(s)\Gamma(-\beta - s)$ with the number of electron N_e within the shower, and the Gamma function $\Gamma(z)$.

The Lateral Distribution Function plays a crucial role in understanding the characteristics and behavior of extensive air showers, and it is a fundamental tool in the field of cosmic ray physics. Nevertheless, the formulation of the LDF can vary depending on the particular observables being considered and the specific context of the study. Different experiments and analyses may focus on different aspects of the LDF or employ alternative approaches.

2.2 The Pierre Auger Observatory

The Pierre Auger Observatory is a leading international scientific facility designed to investigate the origin and properties of UHECRs. It is located in Mendoza, Argentina, and is the current largest cosmic ray observatory in the world. Named after the French physicist Pierre Victor Auger, the observatory has made significant contributions to the field of astroparticle physics since its commencement. The primary goal of the Pierre Auger Observatory is to study cosmic rays, with an energy larger than 100 PeV.

2.2.1 The infrastructure

Over the Pampa Amarilla region, a 1,400-meter-high plateau in Argentina, there exists an array of water-Cherenkov detectors, the surface detector (SD), incorporated with several telescopes, the fluorescence detector (FD), at 4 locations. The whole site covers a vast area of 3,000 square kilometers. The SD measures the air showers produced, while the FD observes the faint ultraviolet light (UV) emitted by the atmospheric nitrogen molecules excited during the passage of cosmic ray

air showers. The fluorescence technique provides complementary information to the surface detectors enabling a more precise measurement of energy and shower profiles. However, the FD operates for a limited period to avoid background UV light, while the SD works almost around the clock. For comparison, the FD has about six times less operating time than the SD. Therefore, the FD provides energy calibration to the measurement, while the SD gives directional information and better statistics.

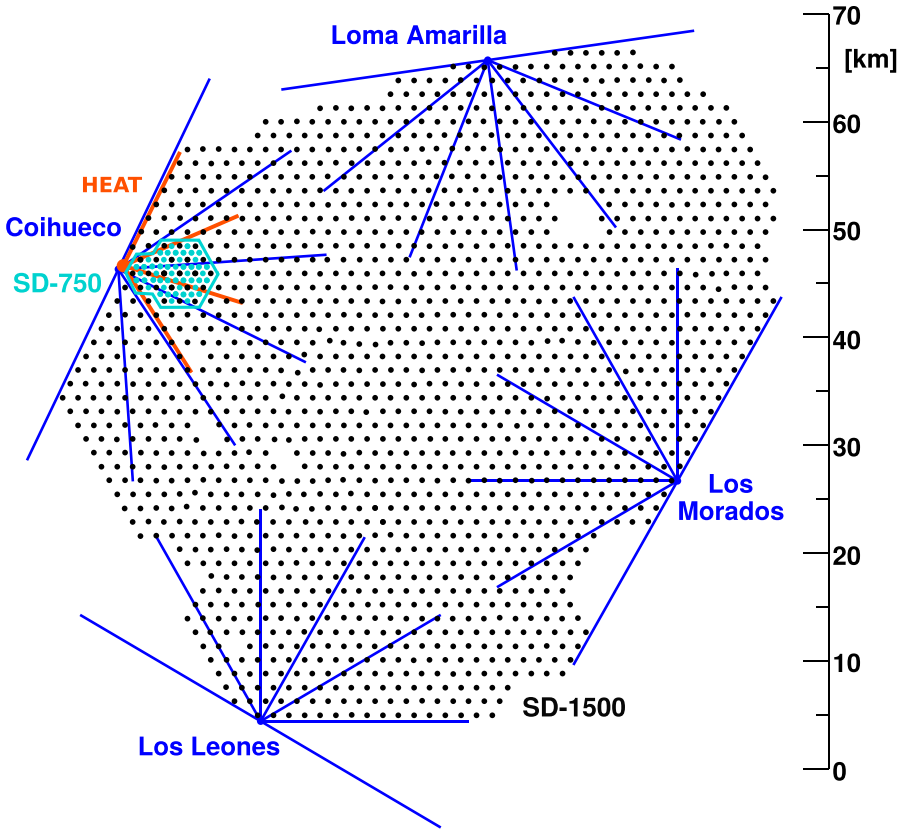

Figure 2.3: Schematic view of the Pierre Auger Observatory. Each dot represents the water tank, while the line-of-sight of each telescope is in between a pair of adjacent blue lines. Near the Coihueco site, there is a denser tank configuration in the cyan line (extracted from [15]).

- **Surface detector (SD)**
  The Surface Detector is a fundamental component of the observatory's infrastructure. It utilizes an array of water-Cherenkov detectors—a cylindrical tank coated with reflective material and filled with 12.2 m^3 of pure water—to detect particles in the EAS induced by UHECR. The motion of ultra-relativistic charged particles in water emits Cherenkov light which is then detected by the photomultiplier tubes (PMTs) attached at the top. Capturing and analyzing the signals reveals the shower's lateral profile, a number density at each slant depth. This information is used to determine the energy and direction of the cosmic ray that initiates the air shower.
  Figure 2.3 indicates the arrangement of 1,660 detectors depicted in Figure 2.4, which are put at about 1,500 meters away from each of the tanks in a triangular configuration, denoted as *SD-1500*. Another smaller yet denser configuration, or *SD-750* from a 750-meter distance, is installed close to the Coihueco site.

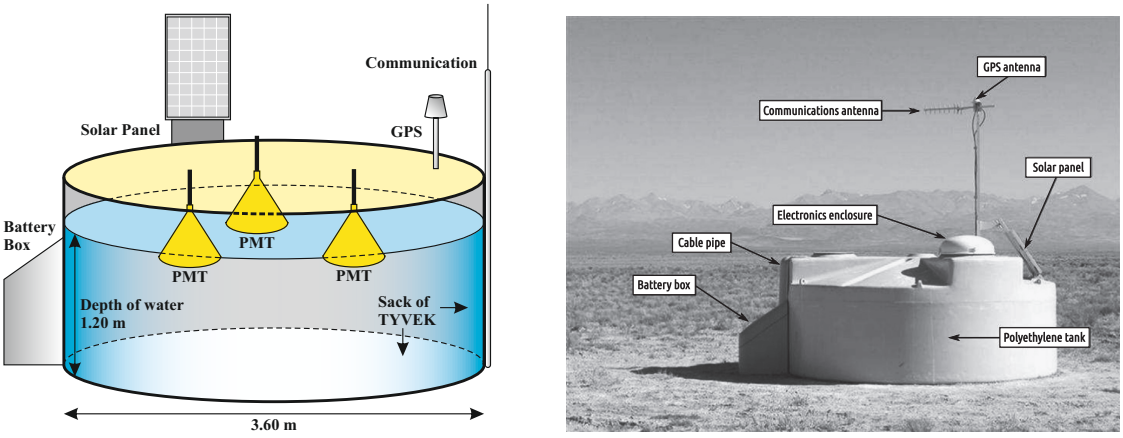

Figure 2.4: Left: Interior view of the surface detector (extracted from [16]). Right: Exterior view of a water tank of the SD (extracted from [3]).

- **Fluorescense Detector (FD)**
  It is a network of telescopes strategically placed around the SD. As can be seen in Figure 2.5, each telescope comprises segmented mirrors, which collect the faint UV light, and a camera that records the images. The mirror has a large reflective area, typically around 13 square meters, to maximize the collection of photons from the EAS. The FD operates during clear and moonless nights when the UV light emitted from the air showers is most visible. It is sensitive to UV light in the wavelength range of 300 to 430 nm, received by 440 PMTs at the camera sensor.
  Initially, there were 24 telescopes each covering 30° both azimuthal and elevation angle, starting from 1.5° altitude. Having 6 telescopes per station, as shown in Figure 2.5, gives the 180° vision to the SD. Later, 3 telescopes called the High Elevation Auger Telescope (HEAT) were installed at the Coihueco station in 2009, as indicated by the red lines in Figure 2.3. This extends the elevation angle to 60° which allows the measurement of shallower showers generated by cosmic rays with energies in $10^{17} - 10^{18.5}$ eV range.

By combining data from both the SD and FD, the Pierre Auger Observatory provides a comprehensive view of UHECRs. This hybrid-detection approach allows scientists to investigate the origin and composition of cosmic rays, as well as to explore phenomena related to particle physics and astrophysics at extreme energies. One of the examples is the determination of the cross-section of nucleon-air interaction at 57 TeV [17], about 4 times higher than the energy achieved at the LHC. Furthermore, it provides the opportunity to test new physics theories that are expected to manifest at extreme conditions, such as Lorentz invariance violation (LIV) [18].

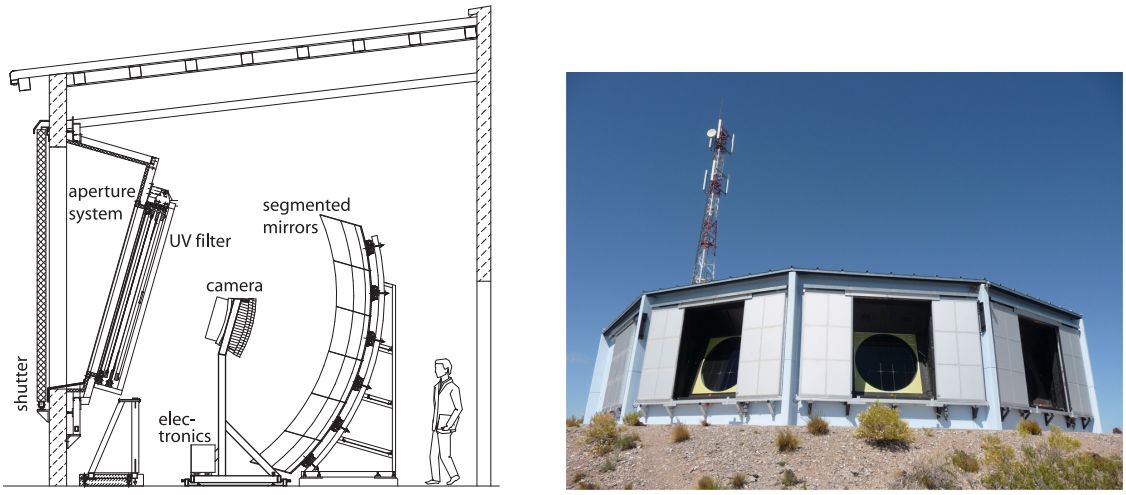

Figure 2.5: Left: Interior view of the fluorescence telescope. Right: Exterior view of the FD station (extracted from [3]).

2.2.2 Direction reconstruction

With the SD, the arrival direction is determined by analyzing the differences in the arrival time between each detector, as illustrated in Figure 2.6, allowing triangulation to estimate the direction of the shower. This requires at least 3 stations to achieve the angular resolution of 1.6°, and with more than 5 stations, the resolution can be improved to 0.9°.

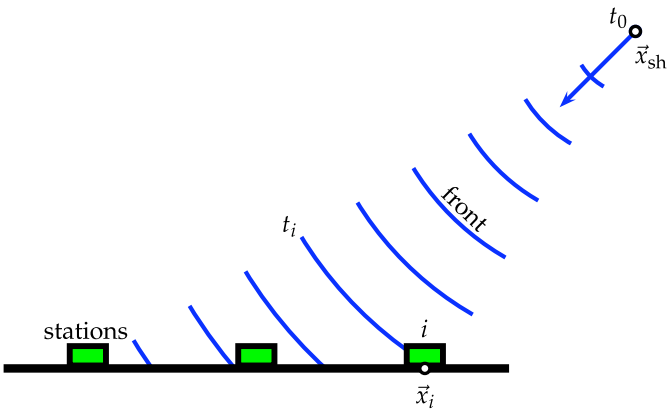

Figure 2.6: Shower front detected by each station at a different time (extracted from [3]).

Another reconstruction is to incorporate both SD and FD measurements as shown in Figure 2.7. By recording the spatial and temporal distribution of the fluorescence light along the shower development, we can use geometry to reconstruct the direction of the incoming primary particle. This technique gives the best angular resolution at 0.6°.

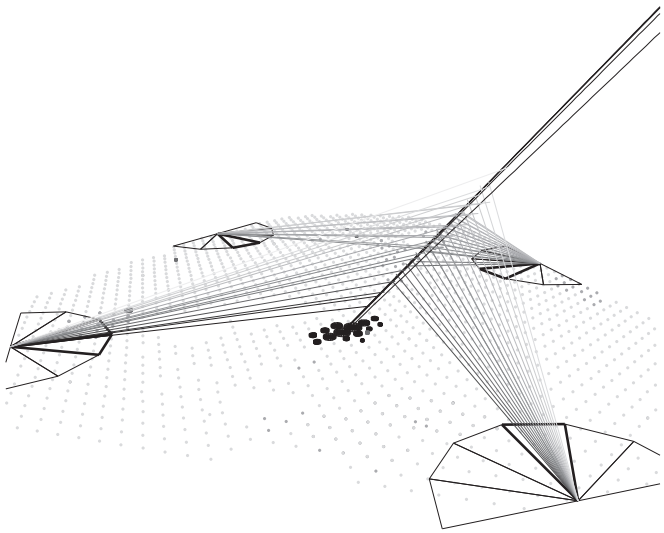

Figure 2.7: Signals received by both SD and FD from the same shower in hybrid mode (extracted from [3]).

2.2.3 Longitudinal profile reconstruction

Light signals measured by the FD are fitted to the Gaisser-Hillas function (see Equation 2.3) to reveal the longitudinal distribution of the shower. By knowing the geometry of the shower, one can convert the arrival time of each signal to the slant depth. However, the measured light can come from other sources, e.g. Cherenkov radiation, and multiply scattered light; thus, many corrections have to be done before we get to the deposited energy. Also, the energy transferred to the fluorescence signal itself depends on the wavelength and various atmospheric conditions. The whole methodology is nicely presented in [19]. The fit presented in Figure 2.8 allows us to determine the maximum depth ($X_{\max}$) which is an important parameter for the composition analysis.

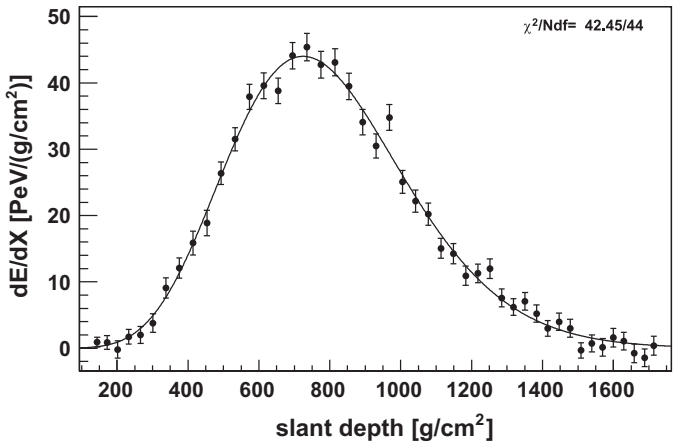

Figure 2.8: Longitudinal profile of a shower, together with the fit of Equation 2.4 in solid line. Maximum depth is obtained from the fit function (extracted from [3]).

2.2.4 Energy reconstruction

The energy can be derived using only single or combined data from those detectors. Typically for the SD, the size estimator $S(1000)$—in the Vertical Equivalent Muon (VEM) unit—is extracted using LDF fit, e.g. Equation 2.4, of the event recorded by SD-1500. It is the signal at 1000 m from the shower axis which is claimed to have the lowest uncertainty [20]. Then it will be corrected to S_{38}, the size estimator as if the shower had a zenith angle at 38°, by the Constant Intensity Cut (CIC) method [21] to eliminate the dependence of the zenith angle. The estimator is then converted to energy using the FD energy calibration. The relation between these two parameters is in the power-law form, as shown in Figure 2.9:

$$E_{FD} = AS_{38}^{B}. \tag{2.5}$$

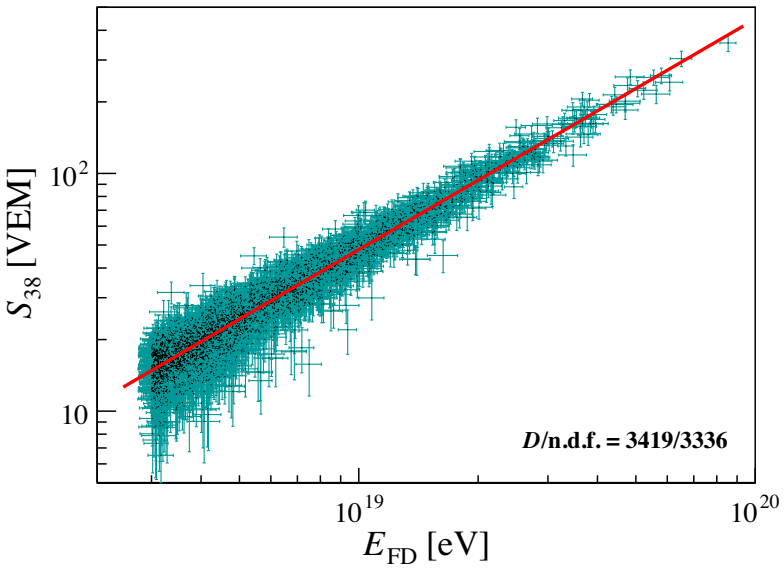

Figure 2.9: Correlation plot of estimator S_{38} and energy E_{FD}. The solid red line indicates the best fit of Equation 2.5, together with the goodness of fit (D) per degree of freedom, $n.d.f. = N - 2$, in the bottom right (extracted from [22]).

The E_{FD} is retrieved by integrating the longitudinal profile, plus the muonic and neutrino sector which is invisible to the FD [23]. This methodology also applies to the SD-750 array, which has different estimators: $S(450)$ and S_{35} with the same definition. However, this only applies to showers with a zenith angle smaller than 60°. For very inclined showers, Monte Carlo simulations are involved to infer the estimator for distorted signals due to the Earth's magnetic field.

2.3 Highlighted discoveries

2.3.1 UHECR spectrum above 2.5 EeV

The Pierre Auger Collaboration has confirmed several findings in their report of the latest measurement of the UHECR spectrum [22], including ankle flattening, changes in the spectral index beyond the ankle around 5 EeV, and abrupt drop at 50 EeV. Here the spectrum is fitted from a series of smoothed broken power-law functions, as shown in Figure 2.10:

$$J(E) = J_0 \frac{E}{E_0}^{-\gamma} \prod_{i=1}^{3} \left[1 + \left(\frac{E}{E_{ij}} \right)^{1/w_{ij}} \right]^{w_{ij}(\gamma_i - \gamma_j)} \tag{2.6}$$

where ij denotes the consecutive interval.

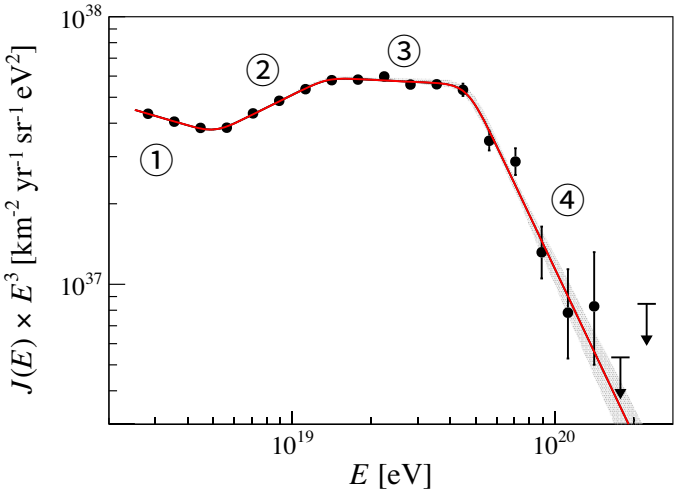

Figure 2.10: Scaled UHECR energy spectrum. The red solid line is derived from Equation 2.6 with the fitted parameters presented in Table 3 of [22]. The shaded band represents the fit uncertainty (extracted and modified from [22]).

Two competing models explain the flattening of the spectrum at the ankle; the dip model [24], and the mixed composition model [25]. The first one deals with the pair-production of the background photons by the pure high-energy proton, while the latter uses multiple particle spectra that result from the transition of galactic to extragalactic origin. As of now, many experimental results, e.g. the following section, agree on the multiple-component model which is assumed for the analysis [26, 27].

The strong spectrum suppression at above 50 EeV is generally explained by the interaction with the CMB via photodisintegration (for heavier nuclei) and photopion production. This was initially discovered separately by Greisen [28], Zatsepin, and Kuzmin [29], later called the GZK effect. However, regarding the modelled injection spectrum, the results of the spectral fit suggest the cut-off at low rigidity [26, 27]. It appears that the potential source, such as active galactic nuclei, is responsible for the suppression, rather than extragalactic propagation.

2.3.2 Energy dependence in UHECR penetration

From the Heitler model in Section 2.1.1, we see that the maximum slant depth depends on the logarithm of energy as well as the mass of the incoming primary. The latter can be explained by a simplified analogy: a cosmic nucleus with energy E and mass number A is conceptualized as A protons, each with an energy of E/A. This gives an implicit relation between $X_{\max}$ and the logarithm of the mass number ($\ln A$). Also, collections of particles reduce the variation in the atmospheric depth. Consequently, heavier nuclei will exhibit lower atmospheric depth and less deviation at the same energy compared to the lighter kind.

Hence, the average and dispersion of $X_{\max}$ distribution can be regarded as the observables for the mass number A. The formulation is derived and presented in [30] as the simple linear relation of the two observables and the logarithm of the nuclear mass $\ln A$:

$$\begin{aligned} \langle X_{\max} \rangle &= \langle X_{\max} \rangle_p + f_E \langle \ln A \rangle \\ \sigma^2 \left(X_{\max} \right) &= \langle \sigma^2_{\text{sh}} \rangle + f_E^2 \sigma^2 \left(\ln A \right) \end{aligned} \tag{2.7}$$

where $\langle X_{\max} \rangle_p$ is the average depth for proton primary, $\langle \sigma^2_{\text{sh}} \rangle$ is the average of $X_{\max}$ variance among primaries, and f_E encodes the hadronic interaction model which is the energy-dependent parameter.

Figure 2.11 presents the energy evolution of these two observables derived from the measurement of the Pierre Auger Observatory, where the transition from lighter to heavier composition is seen at around 4 EeV. The single-composition predictions from 3 different hadronic interaction models; EPOS-LHC [31], Sibyll 2.3c [32], and QGSJetII-04 [33], are also presented for comparison.

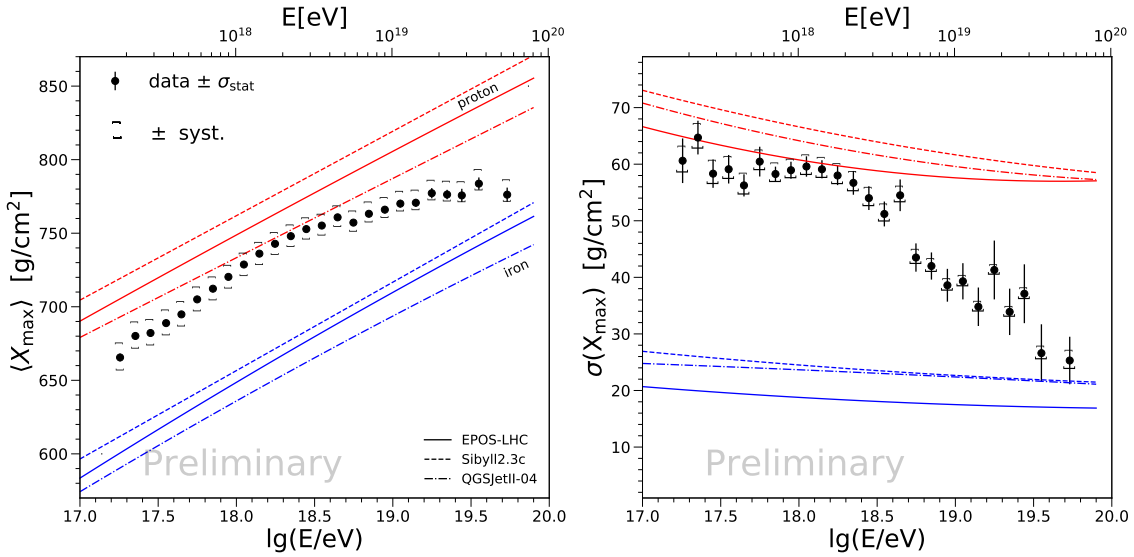

Figure 2.11: Energy evolution of the first and second moment of $X_{\max}$ distribution. The black dots with the errorbar represent the measurement, while those sets of red and blue lines represent the expectation from the Monte-Carlo simulation of 100% proton and iron primary, respectively (extracted from [34])

This result excludes both pure-composition and light-composition hypotheses with very high significance which support the extragalactic UHECR hypothesis. The

caveat is on the hadronic interaction at UHE range where the model is deduced from the experiment at a much lower energy.

2.3.3 Dipolar distribution of UHECR flux above 8 EeV

In 2017, the Pierre Auger Collaboration reported the directional anisotropy of UHECR, visualizing it as a dipolar distribution based on the integrated cosmic ray flux, starting from the minimum energy at 8 EeV [6]. Shown in Figure 2.12, they found that the direction of the dipole, toward the galactic coordinate $(l, b) = (233°, -13°)$ with 6.5% amplitude and 5.2σ significance [6], is off the galactic center.

Apart from this, the dipole direction of the galaxy distribution from the infrared survey 2MRS [35] is nearby, and has the direction within the possible region considering magnetic deflection [36]. This finding supports the extragalactic sources hypothesis as the alignment of the dipole does not conform to what would be expected from galactic emission, where a signal is predominantly populated from the galactic plane.

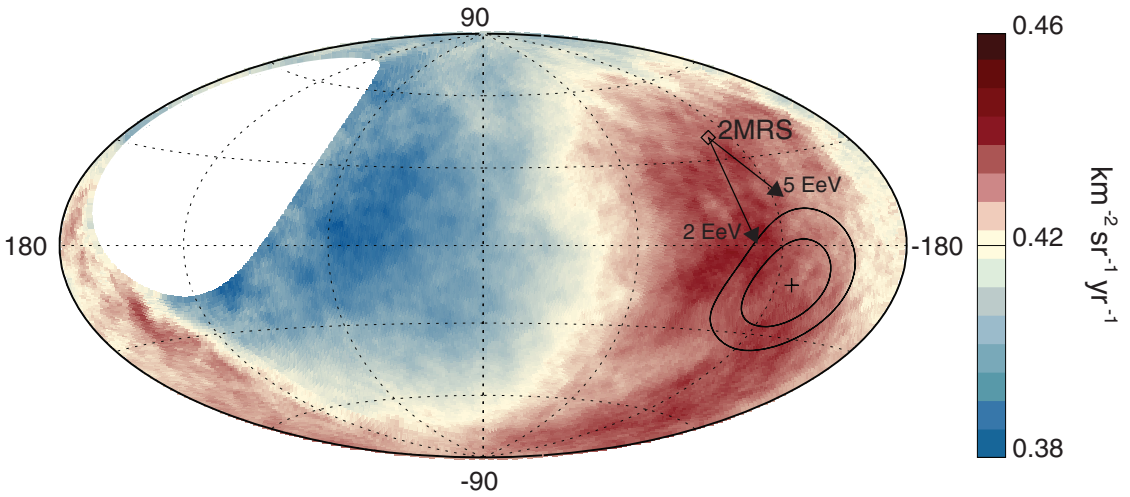

Figure 2.12: A smoothed flux map with a 45° top-hat function of cosmic ray above $E \geq 8$ EeV in galactic coordinate. The reconstructed dipole direction is indicated by the plus sign with 1- and 2-σ boundary. The tip of the arrow represents the deflected direction of the source in the 2MRS catalogue due to the galactic magnetic field with different rigidities (extracted from [6]).

Furthermore, as depicted in Figure 2.13, the UHECR flux demonstrates a stronger dipole amplitude as energy increases, accompanied by a larger phase shift from the galactic plane [37]. This characteristic is absent in cosmic ray energies below the EeV scale. This finding strongly supports the extragalactic origin of UHECR.

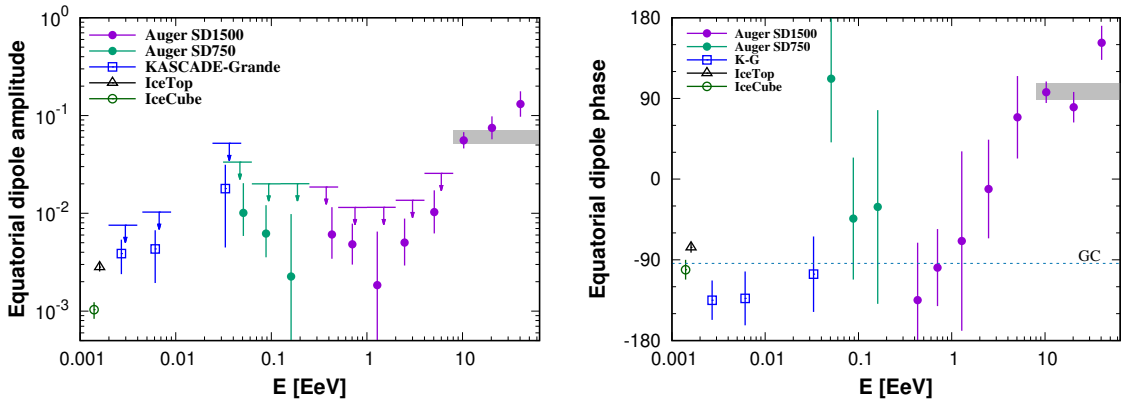

Figure 2.13: Evolution of the dipolar distribution over energy. (extracted from [37]).

2.3.4 UHECR composition anisotropy found above 5 EeV

Later in 2021, regarding the flux measurement, the nuclear composition analysis revealed the anisotropy with a hamburger-like distribution. This indicates that cosmic rays detected in the direction of the galactic plane region contain a statistically different proportion of nuclei, which are heavier compared to those detected in the galactic halo. The composition map in Figure 2.14 explains the composition using

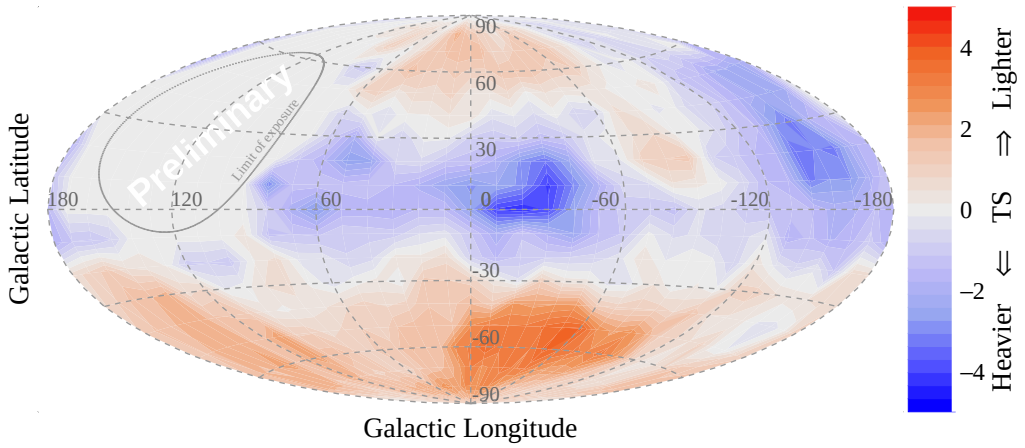

Figure 2.14: t-statistics map of composition analysis (extracted from [7]).

Welch's t-test [38]. The test computes the difference in the first moment of the energy-independent observable, $X'_{\max} = X_{\max} - \langle X_{\max} \rangle_{\mathrm{Fe}}$, between the region around an interested direction and the rest. The general formula to find the test-statistic value is:

$$t = \frac{\langle X_1 \rangle - \langle X_2 \rangle}{s_\Delta}; \quad s_\Delta = \sqrt{\frac{s^2(X_1)}{N_{X_1}} + \frac{s^2(X_2)}{N_{X_2}}}, \tag{2.8}$$

where s_Δ is the combined error of the two compared variables. In this thesis, we try to investigate how strong the magnetic field is going to affect the composition distribution based on the uniform extragalactic source distribution. The composition mapping procedure mentioned in [7] is adopted and will be given in detail in Chapter 4.

Chapter 3

Propagation of UHECR in the Galactic Magnetic Field

Many studies, for example, [26, 39, 40], constrain the UHECR model with many hypotheses altogether, i.e., source distribution, injection spectrum, extragalactic propagation, and galactic deflection. In this thesis, the author is interested in the effect of the galactic magnetic field on the observed mass anisotropy. To tackle this problem, the inside-out approach is discussed: factors affecting the UHECR outside the influence of the GMF are assumed with the simplest scenarios. This will keep the magnetic deflection the only factor for the anisotropy.

As charged cosmic rays travel through interstellar magnetic fields, they experience a series of deflections that can alter their original trajectories. This deflection is explained theoretically in terms of the Lorentz force in the absence of an electric field, $\vec{F} = q\vec{v} \times \vec{B}$. Since it is the only force exerted on charged cosmic rays, these deflections are deterministic: if the initial state is known, then both the final state and the path taken by the particle are also known. However, as will be discussed later in the text, it has to be done by using simulations.

In this work, CRPropa [41], the state-of-the-art framework for UHECR simulation is being used. The differential equation solver is implemented in the package for solving the equation of motion of cosmic particles in the presence of a magnetic field where they are deflected due to the Lorentz force. Since there are various magnetic field models presented in the literature [36, 42, 43], however, the widely-used model named JF12 (abbreviation for Jansson & Farrar's model published in 2012 [36, 43]) is adopted. A glimpse into the field parameterization and structure is explored in the following section.

3.1 Galactic magnetic field model

As we know cosmic rays are charged particles, their paths bend in the magnetic field because of the Lorentz force. Thus, the alteration of the trajectories depends strongly on the magnetic field model. Many publications, e.g. [44, 45], present an overview of the methodology and relevant observations to measure the galactic

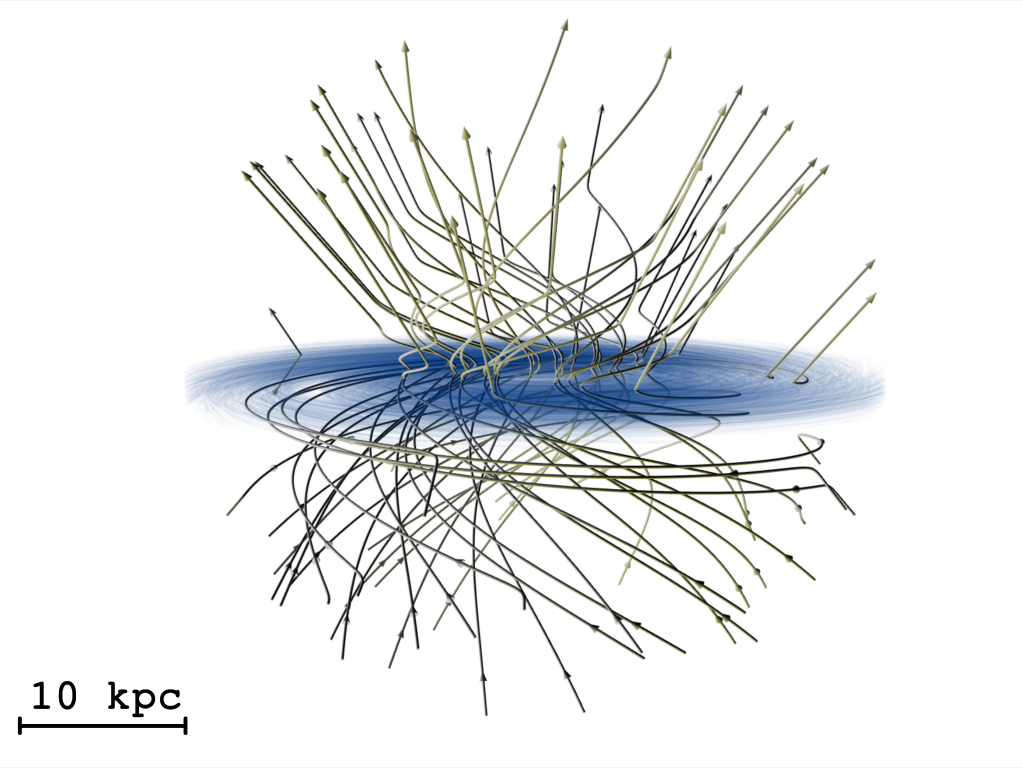

Figure 3.1: Field line representation of the JF12 model. The arrow line represents the halo field, while the thinner blue-ish line represents the disk field (modified from [46]).

magnetic field. The flux density of the galactic field is generally in microgauss (μG)[1] order of magnitude, while the other region with higher gas density, e.g. gas clouds or close to the galactic center, can reach 1000 times stronger.

Several models have been suggested to explain the configuration of the field, where they perform the fit with a large data set that contains multiple tracers of the magnetic field [36, 42, 43]. However, in this study, the JF12 model is adopted due to its superior goodness-of-fit value to the observations, including Faraday rotation and polarized synchrotron radiation. These observations encode the radial and tangential components of the magnetic field, respectively.

The JF12 model deconstructs the field into three components: the large-scale regular field, the large-scale random field, and the small-scale random field. Each of the components is derived independently as it contributes differently to each tracer. These three components give the global parametrization of the field defined in Cartesian coordinates, with the galactic center at the origin. The field is restricted in the sphere of a 20 kpc radius, where the region beyond and inside a concentric sphere of a 1 kpc radius is zero. The latter is neglected simply due to a lack of statistics. The three-dimensional field line of the large-scale component is displayed in Figure 3.1, contained in a sphere with a radius of 20 kpc.

The regular field represents the colossal structure that reveals the overall structure of the galaxy, including the galactic disk, galactic halo, and the inhomogeneous

[1] 1 μG= 10^{-10} T

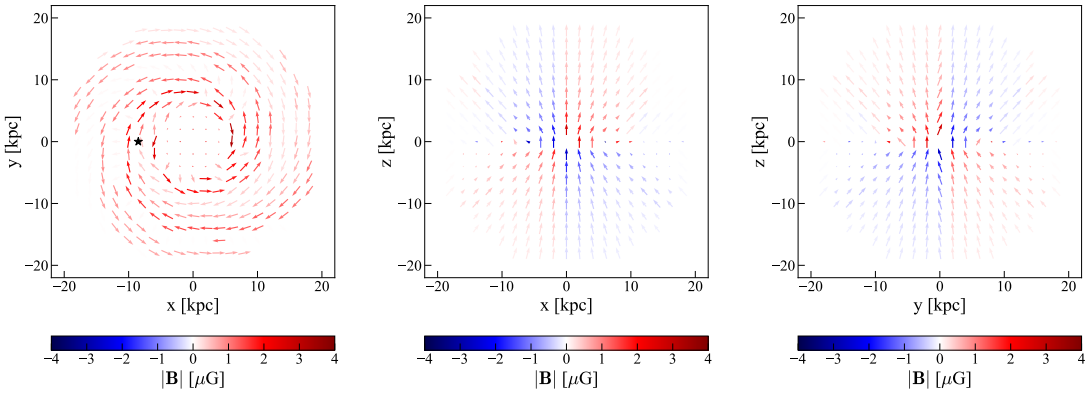

Figure 3.2: Projections of the regular field of the JF12 model in the coordinate planes. The color opacity represents the magnitude of the field, while red/blue indicates the direction of the third axis, with blue/red means the inward/outward of the paper. On the left figure, the position of Earth $(x, y, z) = (-8.5, 0, 0)$ kpc is denoted by a star.

field commonly known as the X-field. The disk is defined in the x-y plane with the position of the Sun at $x = -8.5$ kpc. The disk is split radially into 2 regions: 3 kpc $< r <$ 5 kpc and $r >$ 5 kpc. The inner region field is azimuthal with homogeneous strength at 0.1 ± 0.1 μG. The outer region displays the spiral feature of the galactic arm with 8 sections, each with independent strength and direction. The half-thickness of the disk is 0.40 ± 0.03 kpc, defined as the transition width to the halo field in the logistic function. The galactic halo is modelled by the toroidal field with exponential decrease along the z-axis that is asymmetric between the northern and southern hemispheres. The inspiration for the out-of-plane component is from other galaxies, where they observed an 'X' shape in radio observation. Figure 3.2 visualizes the model with the inheritance of the galactic arm configuration in the spiral disk field. As seen in the vertical slices, the field curls in different directions between the northern and southern halo.

The large-scale random field, or 'striated' random field, displays the anisotropy in the regular field. The field orientation aligns with the regular field; however, over a coherent length of approximately 100 pc, the direction can either be anti-parallel or parallel, while the strength is random. The field is proportional to the regular field so that the relative strength is defined as $\mathbf{B}^2_{\text{stri}}/\mathbf{B}^2_{\text{reg}} = 1.36 \pm 0.36$. Whereas local phenomena, such as supernovae, induce the small-scale random field, this component is excluded from the fit.

Using this three-dimensional model, one can determine how a cosmic ray propagates by solving the equation of motion. However, due to the randomness of the entering point and the direction of a cosmic ray, and also the random component of the GMF, the analytic solution for the trajectories is not realized. Therefore, the propagation in the magnetic field has to be done using numerical simulation.

3.2 Magnetic lensing

The galactic magnetic field can be regarded as a lens that bends the trajectory of the particle, causing flux magnification/reduction and also the illusion of the same source in many directions [47, 48]. This concept leads to a new way of simulating propagation in the magnetic field. Bretz *et al.* [39] outlines the production of the magnetic lens, which will be briefly given in this section, followed by the application.

3.2.1 Production of the magnetic lens

Generally, the traditional simulation, or 'forward tracking', is done by numerically solving the equation of motion, given the initial states of the cosmic ray in phase space and the magnetic field model. Unfortunately, this is computationally expensive; thus, the conventional 'lensing' method is introduced. By construction, the particle trajectory is deterministic since the energy loss due to the synchrotron effect is minuscule (see Appendix A). Consequently, if the antiparticles are released at Earth, they will follow the paths that real particles could take in reverse. This technique is called backtracking, and all of the simulated particles will have contributed to the observation at Earth compared to the typical simulation that discards many pass-by events.

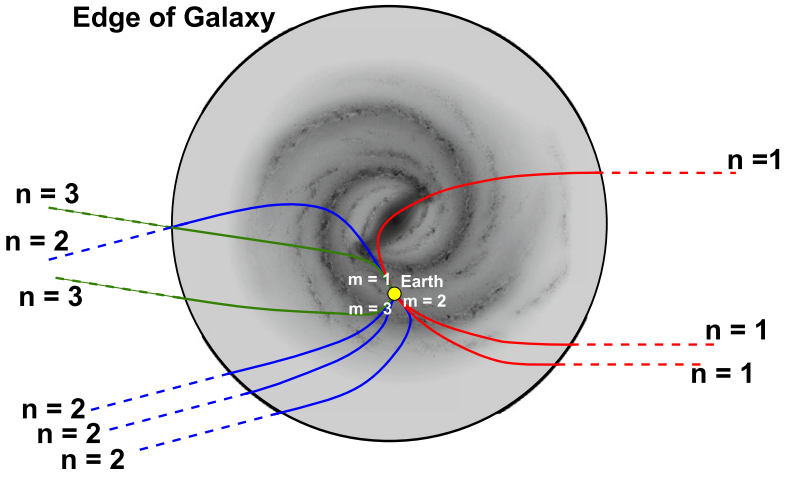

Figure 3.3: Tracks of anti-particle emitted from Earth with direction **m** through the magnetic field and leaving the galaxy with direction **n** (extracted from [39]).

In Figure 3.3, a number of anti-particles, with rigidity defined as $R_i = E_i/Ze$ where Z is the charge number of the nuclei, are released with initial direction **m**. Propagation under the magnetic influence leads to many possible leaving directions **n**. This information will be used to make the lens.

From the backtracking data, one can construct a matrix $\mathcal{L}^i$ with each element in a row **m** representing the probability from each direction **n** from the edge of the galaxy. The arriving flux distribution P_{E} is found by simple matrix multiplication:

$$P_{\mathrm{E}} = \mathcal{L}^i \cdot P_{\mathrm{G}} \tag{3.1}$$

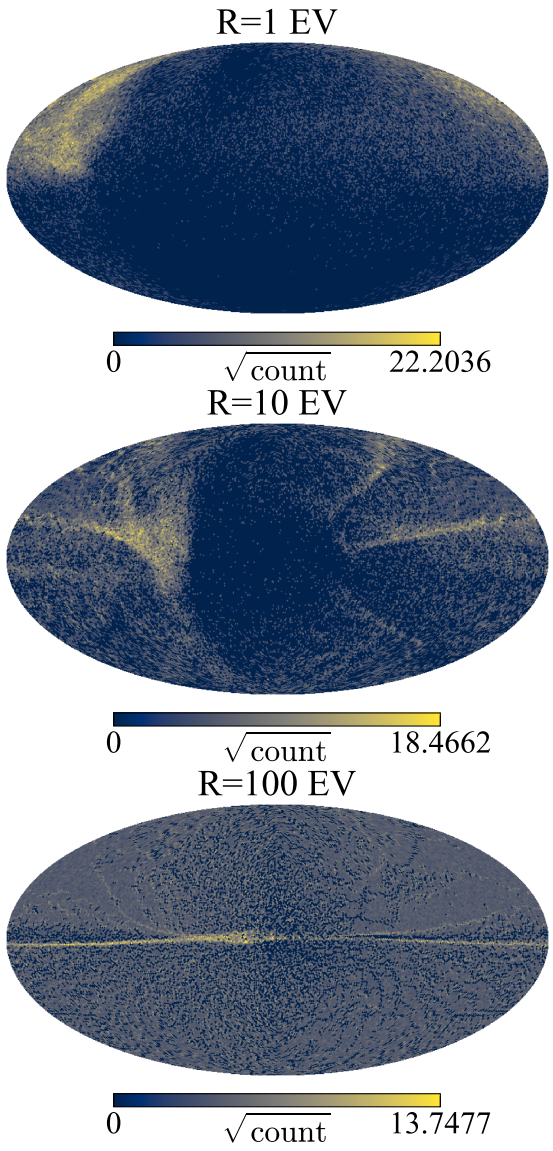

Figure 3.4: Back tracking count map in Mollweide projection. The count per pixel is on the square root scale for better visualization.

where P_{G} is the incoming probability distribution at the edge of the galaxy. Each element in $P_{\mathrm{G/E}}$, defined in a 1-dimension array, represents the arbitrary measurement that comes from the direction according to the Hierarchical Equal Area isoLatitude Pixelation (HEALPix[2]) [49] of 49,152 pixels. This pixelation scheme ensures an equal solid angle per pixel, and the ordering intrinsically encodes the coordinate system. This way, the lensing matrix is simply defined in a 2-dimension array.

Figure 3.4 presents an example of the backtracking results for $R = 1, 10, 100$ EV. These maps are created by ejecting 10^6 particles isotropically at Earth's coordinate through the GMF defined in Section 3.1. These maps are then converted to the lensing matrix using Equation 3.1.

In this work, the magnetic lenses available for the JF12 model are adopted, which

[2] `http://healpix.sourceforge.net`

can be accessed through the CRPropa website[3]. It provides the matrix from $R = 10^{17.00} - 10^{20.48}$ EV with 0.02 spacing in $\log_{10}(R)$, which supports the lensing of ultra-high-energy iron nuclei with a minimum energy of 2.6 EeV. By employing this technique, the computational cost is significantly reduced.

3.2.2 Forward propagation using magnetic lens

Since the propagation of UHECR in the magnetic field is considered energy-lossless, the lens matrix can be defined for a single rigidity. Therefore, to include the propagation with the spectrum, the resulting flux map is the superposition of each individually applied lensed map at each rigidity. This leads to the deformation of the measured energy spectrum on Earth [47].

To demonstrate the effect of the lens, a set of random arrival directions is drawn from the Fisher distribution [50], with the galactic center as the central point of the distribution, and the lens is applied using Equation 3.1 for $R = 1, 10, 100$ EV, as presented in Figure 3.5. The results show that the magnetic field redirects the path of the particle. For a low rigidity, it is interesting that the particle initially from the direction of the galactic center (the center of the plot) could be detected in the opposite direction (left/right most of the plot) at Earth. Furthermore, the lens matrix of each rigidity gives different levels of spread: the fuzziness reduces with increasing rigidity.

From this simple example, some features of the galactic magnetic field are inferred: it reduces the observed flux and shuffles the arrival direction with different strengths depending on the particle's rigidity. It means that the particle with low rigidity experiences stronger magnetic deflection. This effect is also directional dependent, as discussed in [48], where different incoming directions provide different levels of deflection. In the following section, the isotropic source UHECR hypothesis will be extensively discussed.

[3] `https://crpropa.github.io/CRPropa3/pages/AdditionalResources.html`

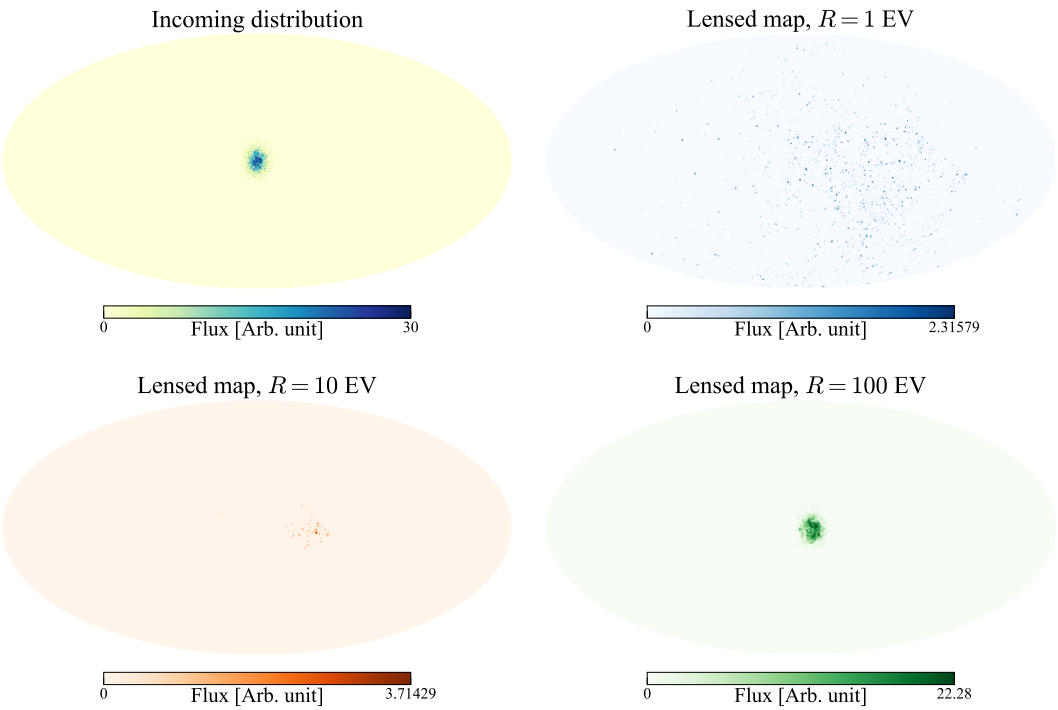

Figure 3.5: Top left: An example of the incoming distribution from the direction of the galactic center. Top right and bottom left and right: The lensed distribution after applying the lens matrix for $R = 1, 10, 100$ EV, respectively. These maps are plotted in Mollweide projection with galactic coordinates.

3.3 Propagation of the isotropic source distribution

Modeling the extragalactic propagation needs to consider many assumptions (see [39]). However, the description of source distribution and the extragalactic magnetic field model are not easily determined. In this work, those complications are disregarded and only the effect of the galactic magnetic field, which has been extensively investigated and well understood, is considered.

Here, the spatial model of the source is assumed for an isotropic case, and single rigidity for the spectral distribution, equivalent to a proton with monochromatic spectrum. The isotropic incoming or 'unlensed' distribution is made by uniformly drawing a set of the ordering numbers of the map from 0 to 49,151. This simulates the extragalactic hits from each direction according to HEALPix pixelation of order 6 [49], equivalence to $4\pi/49152$ steradians per bin or about 1° spacing. Then, the simulated set is binned into a histogram. The value of the histogram then represents the number of hits per direction. This will be transformed into the arrival or 'lensed' distribution using the method from the previous section. The latter represents the relative average flux of cosmic rays with rigidity R that reaches Earth.

An example of 10^6 incoming UHECRs with isotropic source distribution, before and after applying the magnetic lens at $R = 1, 10, 100$ EV, is shown in Figure 3.6. Based on visual observation, the lensed distribution appears to exhibit a higher probability in the galactic center region, which seems to contradict the Liouville theorem: the isotropic arrival distribution is expected from the isotropic incoming distribution

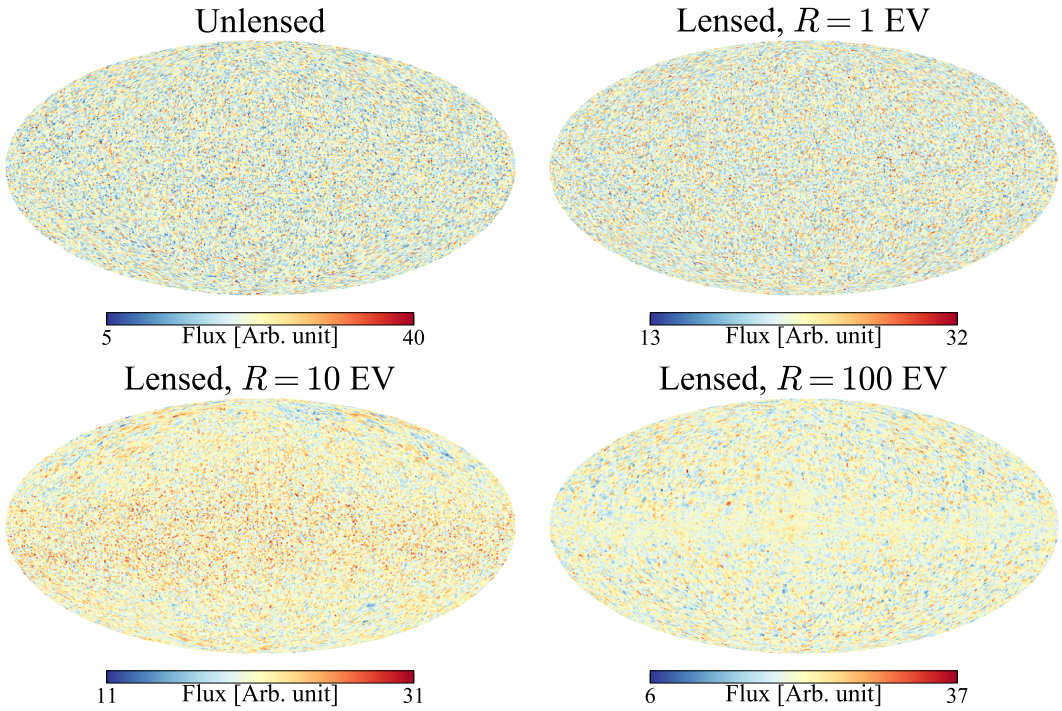

Figure 3.6: Top left: Uniform distribution of the incoming cosmic rays. Top right and bottom left and right: The lensed distribution after applying the lens matrix for $R = 1, 10, 100$ EV, respectively. These maps are plotted in Mollweide projection with galactic coordinates.

[47, 51]. This observation will be rigorously examined through numerical analysis in subsequent sections.

3.3.1 Magnetic field effectiveness

In the investigation of the GMF, a source-distribution independent model is adopted to test its effects. Consequently, an isotropic distribution is anticipated for the incoming flux of UHECRs. The value from the incoming distribution is first inspected using histograms. Since the hits are independent, the number of hits per direction follows a Poisson distribution.

In a manner similar to Figure 3.6, a total of 1000×49152 particles are drawn to create the incoming flux map, resulting in an average of 1000 hits per direction. The initial number of particles chosen here is arbitrary but will be further discussed in the text. Subsequently, a histogram is constructed from the incoming map, as illustrated in Figure 3.7. It exhibits Poisson statistics, with $\sigma \approx \sqrt{\mu}$, as expected. However, the histogram of the propagated map with $R = 1, 10, 100$ EV displays different statistics, resembling a normal distribution. This behavior occurs because the number of hits in the incoming map is an integer value, whereas the transformation using Equation 3.1 rationalizes these integers, modifying the discrete counts into a continuous distribution.

Interestingly, upon examining the width of these lensed histograms, one observes a dependence on the rigidity of the magnetic lens. As rigidity increases, the his-

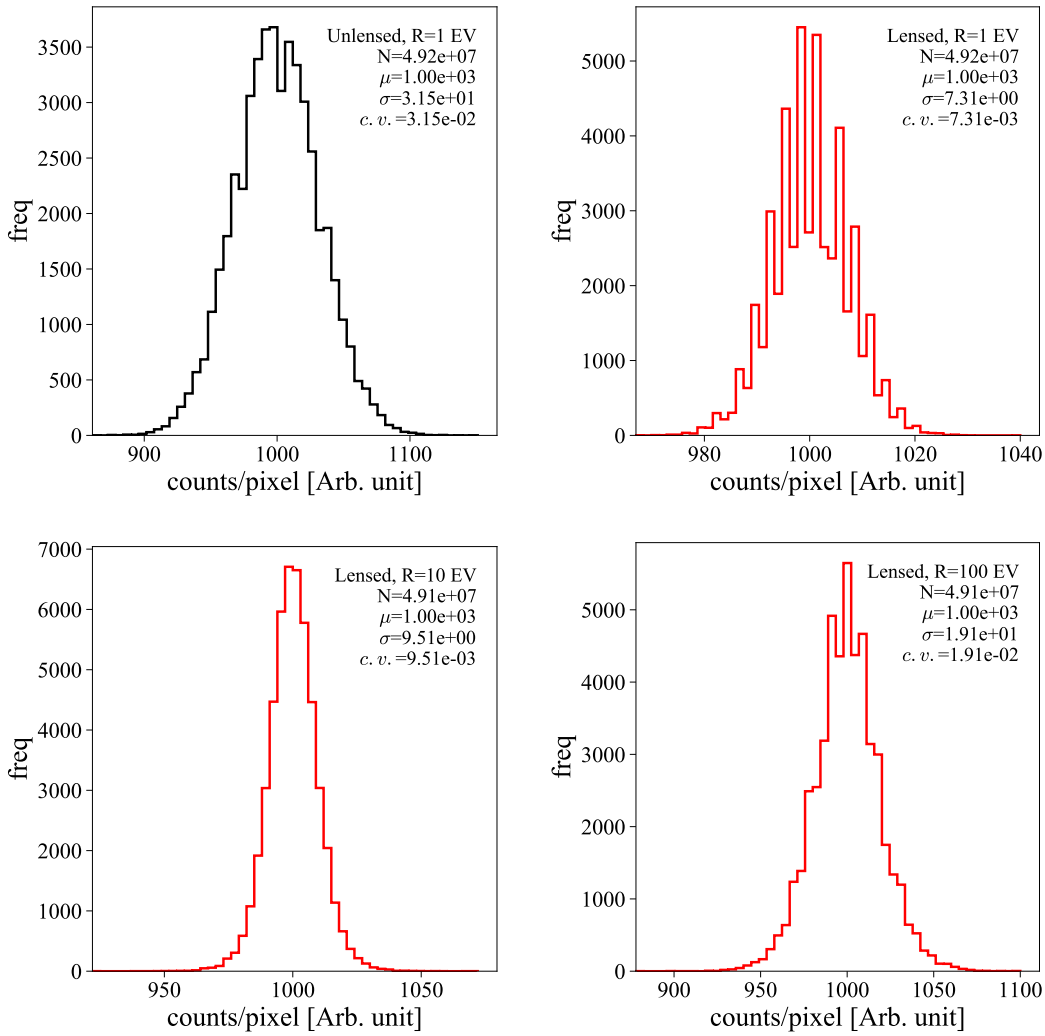

Figure 3.7: Histograms of the flux distribution before (left) and after (right) applying the magnetic lens at $R = 1$, 10, and 100 EV. See Appendix C for other initial numbers.

tograms become wider. This rigidity-dependent effect arises from the isotropization of the magnetic field. For low-rigidity particles, the magnetic field isotropizes the distribution, leading to a smoother relative flux at Earth. To observe this effect as a function of rigidity, the magnetic field effectiveness is defined by the ratio of the coefficient of variation

$$\eta = \frac{c.v._{\mathrm{G}}}{c.v._{\mathrm{E}}} \tag{3.2}$$

with $c.v. = \sigma/\mu$ of the histogram. This compares the shape of the lensed distribution with the unlensed distribution.

From Figure 3.8, the magnetic field reduces the fluctuation by up to 4.5 times of the initial map, for $R < 3$ EV. With increasing rigidity, the effectiveness drops by 3 times. This indicates that the incoming distribution will likely be fully isotropized for $R < 3$ EV. If the two distributions are identical, e.g. in a very high-rigidity case, the effectiveness parameter approaches unity.

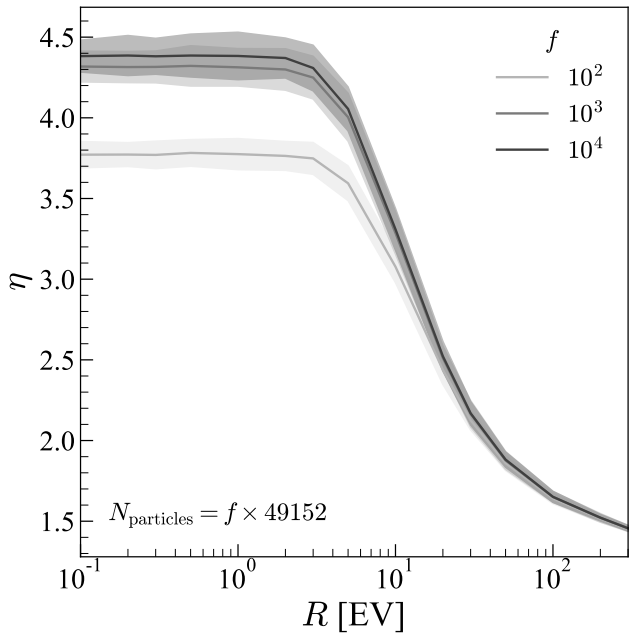

Figure 3.8: Magnetic effectiveness as a function of rigidity, averaged from the 100 simulations of discrete incoming distribution with different numbers of particles. The shaded area is the $\pm 5\sigma$ interval derived from the standard deviation in realization data. It is noted that the total number of initial particles is limited to $f = 10^4$ in the following calculations as it is not statistically different from $f = 10^3$.

To observe the effectiveness parameter for each element, the rigidity is transformed into energy by multiplying the particle's charge Z. The energy dependence of the effectiveness for each selected primary element is depicted in Figure 3.9 using the data set with a multiplication factor of $f = 10^4$. The plot is shifted according to the charge $Z = 1, 2, 7, 14, 26$, resulting in an energy range limit from 2.6 to 300 EeV, constrained by the availability of the magnetic lens.

For the proton, as depicted by the red line in Figure 3.9, the effectiveness decreases as the energy increases, while heavier elements, e.g. iron, have a decrease in effectiveness at higher energy. This behavior can be explained by considering the strength of the Lorentz force: the larger the charge of the particle, the stronger the force. Thus, the difference in magnetic effectiveness at each energy suggests that the UHECR spectrum of each primary particle plays a crucial role in mass anisotropy.

Finally, the effect of different initial numbers of incoming particles is discussed. In general, the incoming particle should be simulated for a significantly large number, e.g., more than 10^9 as being adopted in other works [39, 40]. The effect of changing the initial number is investigated, covering 3 orders of magnitude of the multiplication factor of 49,152. Therefore, in Figure 3.8, the simulation is repeated for each multiplication with 100 sets of data for consistency. Even though a higher number of initial particles is more realistic, the simulation stops at $f = 10^4$ as it already gives convergence to the parameter.

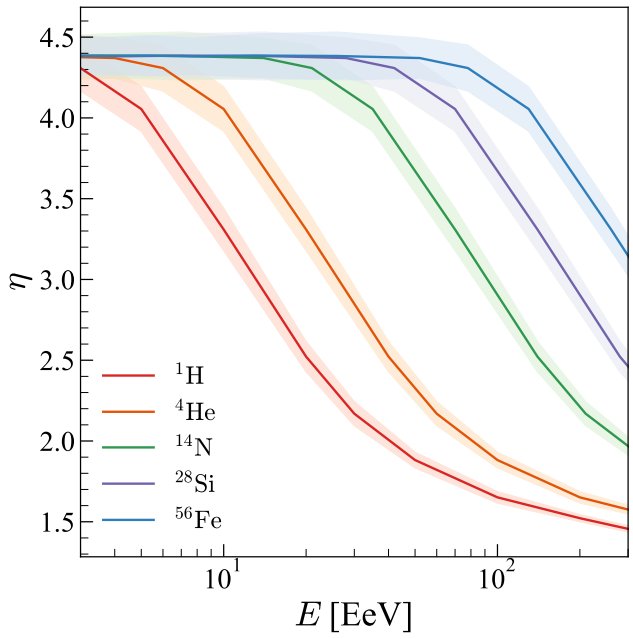

Figure 3.9: The magnetic effectiveness as a function of energy obtained from a simulation of $f = 10^4$ initial particles. Five UHECR species; H He, N, Si, and Fe, are presented with different colors.

3.3.2 Arrival probability as a function of galactic latitude

To illustrate the impact of magnetic lensing on extragalactic particles arriving from various directions, the decision is made to divide the incoming map along the galactic latitude. The motivation behind this approach stems from the significant mass anisotropy observed along galactic latitude, as shown in Figure 2.14. To ensure equal area coverage for each band, the map is truncated by 9 pixels from both the top and bottom. This truncated array is then effectively divided into 19 horizontal stripes, each equally consisting of 2586 pixels. The choice of an odd number of bands allows the central band to lie precisely at the galactic plane. The events that fall into each band will be characterized as arriving from the average latitude ($\overline{\theta}$) of all pixels in the corresponding band.

In this context, the symbols used must be clarified: $\theta_{\rm G}$ represents the galactic colatitude[4] of the extragalactic particles, while θ_E denotes the arrival direction of the propagated particle at Earth. This notion will be used interchangeably with the galactic latitude (b) whose range is between b =90°, or $\theta = 0$ rad, for the North galactic pole, and $b = -90°$, or $\theta = \pi$ rad, for the South galactic pole.

Arrival probability from different incoming direction

For this analysis, 10^5 incoming particles are drawn uniformly for each band, following the same procedure for the whole sky isotropic distribution. This total number is

[4]It is equivalent to the zenith angle in spherical coordinates and can be converted to galactic latitude by $b = \pi/2 - \theta$.

arbitrarily chosen to ensure an unbiased distribution between each part of the sky. An illustration of the selected isotropic band, before and after applying the magnetic lens for $R = 1, 10, 100$ EV, is presented in Figure 3.10. It is evident that the magnetic lens effectively isotropizes this initially biased incoming distribution at low rigidity, with the effect gradually diminishing, as discussed in the previous section.

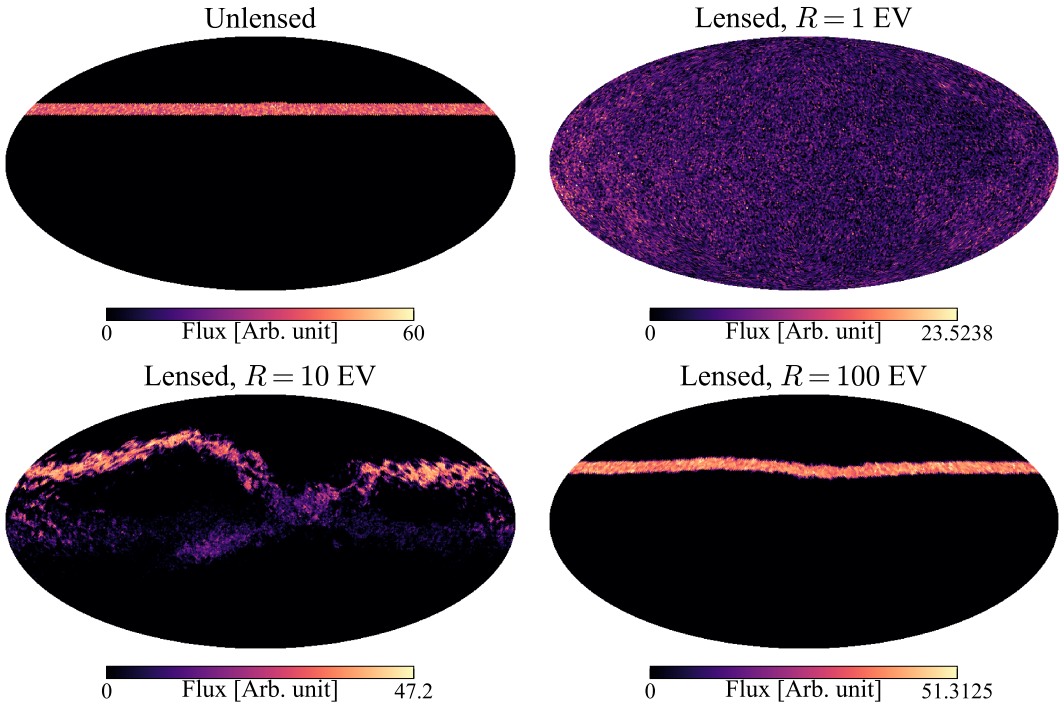

Figure 3.10: Unlensed (top left) and lensed flux maps from isotropic incoming particles with average incoming colatitude ($\cos(\overline{\theta}_{\rm G}) = 0.53$). The map is in Mollweide projection of galactic coordinates.

For each rigidity, when the lensed distributions from every band are combined, a result similar to Figure 3.6 is obtained. This implies that each lensed distribution contributes to a different portion of the sky, but when combined, they collectively yield an isotropic distribution. From the total number of each lensed map from each band, one can consider it as the relative arrival probability from the corresponding band. To determine the arrival probability ($P(\theta_{\rm G})$) from each band, the flux map is normalized by dividing the total arrival flux for each band by the total arrival flux from all bands.

The arrival probability distribution along the galactic latitude is presented in Figure 3.11 for rigidity $R = 1, 10, 100$ EV. It shows that the probability for the bands with $\cos\theta_{\rm G} > 0$, or the above the galactic plane, is higher than the region below the galactic plane. The results suggest that the arriving flux has preferred incoming directions: the northern hemisphere. This result agrees with the flux enhancements in [48], where half of the incoming direction, mostly in the northern hemisphere, contributes to almost all of the flux observed at Earth.

Nevertheless, the probability distribution gradually flattens as the rigidity increases. This is expected as ballistic propagation takes over in the high-energy regime, where every incoming direction has roughly the same probability of arriving at Earth. What is noticeable in the distribution is the peak of probability in the galactic plane

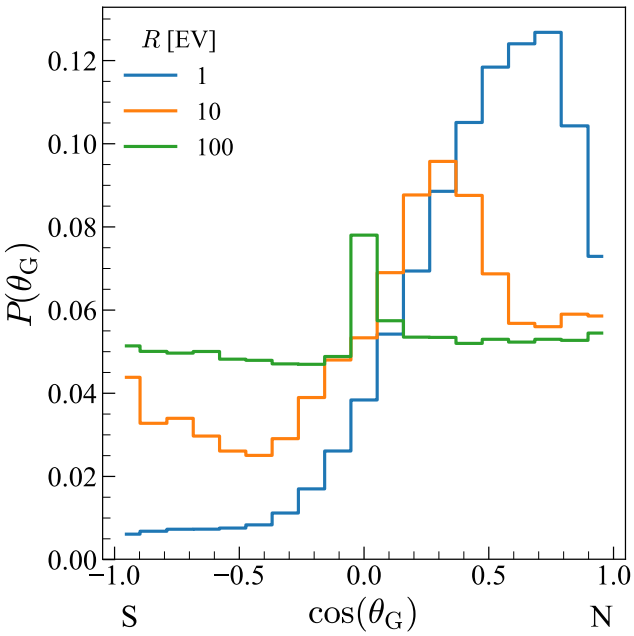

Figure 3.11: Incoming probability distribution from each colatitude band. The cosine function applied to the x-axis is for better presentation. Denoted below the horizontal axis is the direction of the southern (S) and northern (N) galactic poles.

for $R = 100$ EV. This indicates that particles with the incoming direction at the galactic plane have a greater chance of being detected at Earth at high rigidity. This is because the Earth is located in the galactic plane, but not at the galactic center. As the level of isotropization is low at high rigidity, the direction of the galactic plane could be considered a 'head-on' collision, compared to the other latitude band that the particles need to be deflected in order to arrive at Earth. This feature relates to the backtracking data as shown in Figure 3.4.

Directional probability at Earth

Further inspection is made on the arrival or lensed flux map. Using the same method mentioned above, the arrival distribution, for example, in the top right of Figure 3.10, from an incoming distribution of a single band is divided into 19 bands. The sum of each band represents the relative arrival flux at different galactic latitudes of the Earth's sky, denoted by the average galactic latitude θ_E. The directional probability from a given incoming band, $P(\theta_E|\theta_G)$, is subsequently determined by dividing the total count in each band by the total count of the lensed map.

The directional probability distribution along the galactic latitude from an incoming uniform band at $\cos(\theta_G) = 0.53$, or $b = 32°$, is presented in Figure 3.12 for the rigidity $R = 1, 10, 100$ EV. For the lensed distribution as shown in Figure 3.10, the flux is strongly isotropized for low rigidity, which is reflected in the flat distribution, e.g. for $R = 1$ EV (blue line) in Figure 3.12. Again, the expected trend for the increasing rigidity is in agreement with the previous section, where isotropization is much weaker in high rigidity. As rigidity increases, the probability distribution localizes

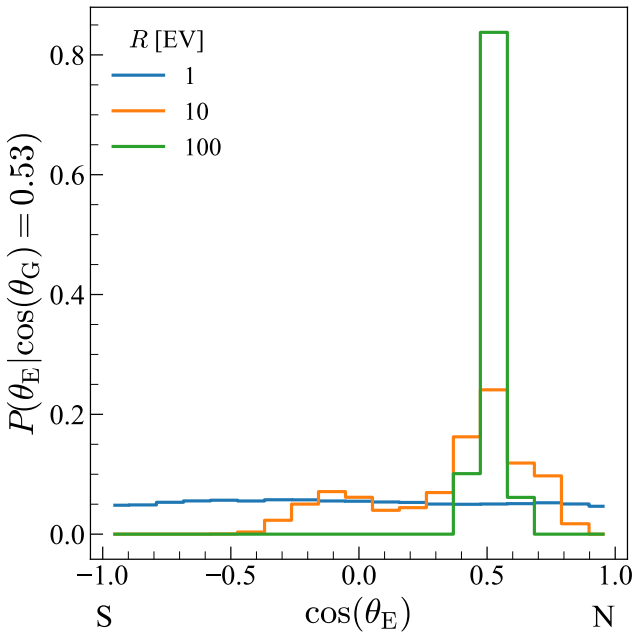

Figure 3.12: Arrival probability distribution from each co-latitude. The cosine function applied to the x-axis is for better presentation. The uniform distribution over the Earth's sky is expected from lower rigidity, while the distribution localizes at high rigidity.

around the same galactic latitude as its incoming band, e.g. $R = 100$ (green line) in Figure 3.12.

Correlation between incoming and arrival direction

Combining the two probability distributions at which the particles enter the sphere of influence and arrive at each galactic latitude band at Earth yields:

$$P(\theta_E, \theta_G, R) = P(\theta_E|\theta_G) \times P(\theta_G) \tag{3.3}$$

This parameterizes the arrival probability as a function of the incoming direction and arrival direction, which helps to constrain the source distribution hypotheses. This probability function is presented in a 2d-histogram in Figure 3.13 for $R = 1, 10, 100$ EV, with the incoming galactic latitude band in the x-axis, while the arriving direction is in the y-axis. From these matrices, one can directly observe the correlation between the source direction and the arrival direction along the galactic latitude. This allows an easier way to hypothesize the source distribution regarding the observed arrival distribution and to roughly estimate the spectrum.

However, the isotropic distribution is still expected in the arrival distribution of the isotropic incoming map, following Liouville's Theorem. If we sum the probability horizontally, along each galactic band at Earth, the cumulative probability yields a nearly identical value, which happens because of the truncated map. The numerical values of the probability matrix are presented in Appendix B.

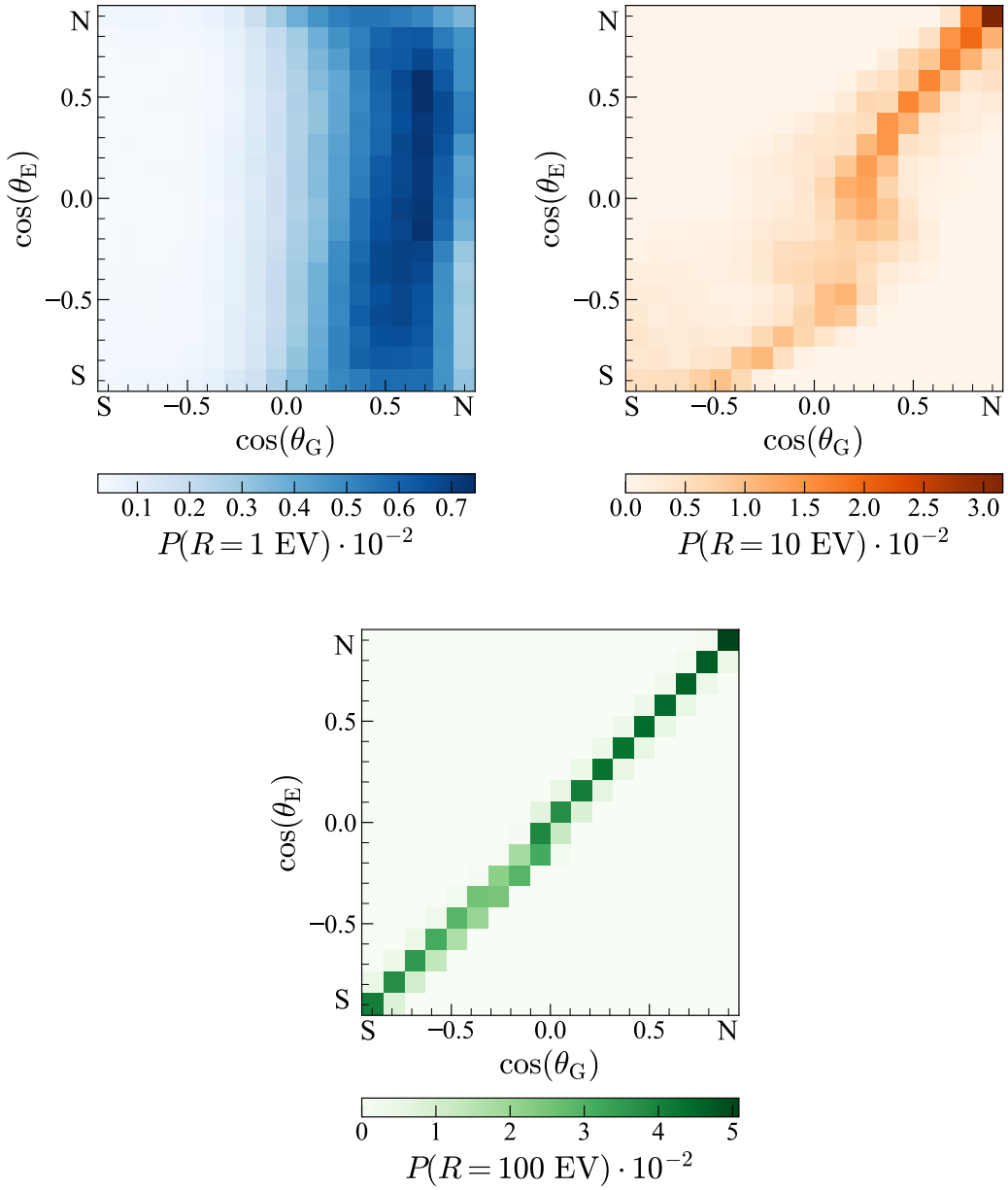

Figure 3.13: 2d-Probability distribution for the arrival distribution. The direction of the southern (S) and northern (N) galactic poles are indicated with both axes. The numerical values are presented in Appendix B.

In this section, a comprehensive analysis of the magnetic field's influence on UHECR propagation is presented. Nonetheless, it is important to note that the lensed map primarily provides the probability of detection in each direction. This distribution will be sampled to create the simulated observational data. This will be discussed in the next section.

3.4 Simulation of detection at Earth

The relative probability provided by the lensed map P_{E} can be considered as the average flux in each direction. To simulate the actual events that could be detected by the Earth-based observatory, events are sampled from this arrival probability distribution. This process is achieved using a random number generator. To facilitate the sampling process, the lensed flux map requires normalization, ensuring that $\sum P_{\mathrm{E}} = 1$. Subsequently, any desired number of events can be arbitrarily chosen, which gives the results following this probability distribution.

The arrival probability map for $R = 50$ EV created from $1,000 \times 49,152$ incoming particles and the sampled map from 10^6 events are shown as an example in Figure 3.14. Notably, the anomalous structure, as previously seen in the lensed distribution, disappears in the sampling data set. This will be investigated in the following.

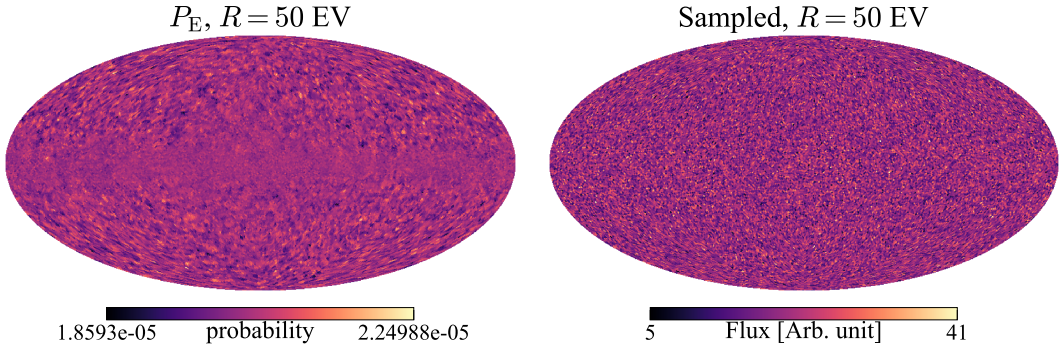

Figure 3.14: (Left) Arrival probability map (Right) the simulated detection map. The fairly anisotropic pattern on the probability map is not imprinted on the sampled map.

3.4.1 Average flux as a function of galactic latitude

Here, the arriving flux map and the sampled flux map are compared. The arrival flux is computed from the lensed map of isotropic incoming distribution with $10^3 \times 49152$ particle at $R = 50$ EV. Then, the sample data set is made for each different number of events, using this arrival distribution as the probabilities associated with each direction. Despite the fact that the rate of UHECR detection is rather small, for sufficient statistics, events are arbitrarily drawn from this distribution at this single rigidity, ranging from $N = 10^5$ to $N = 10^8$. This number is overestimated compared to the total UHECR events from $E > 2.5$ EeV reported by the Pierre Auger Observatory [22].

Both maps are divided into 19 galactic latitude bands, using the same method mentioned in the previous section. Then, the mean and standard deviation of hits per bin in each band are computed. This reveals the distribution of the relative flux of each direction within each band. If there is a difference in the mean of relative flux, then flux anisotropy is observed, and Liouville's theorem is violated. For comparison, the coefficient of variation as in Equation 3.2 is used instead of

the standard deviation. These values then measure the relative fluctuation of the number of hits per direction in each band. The results are given in Figure 3.15.

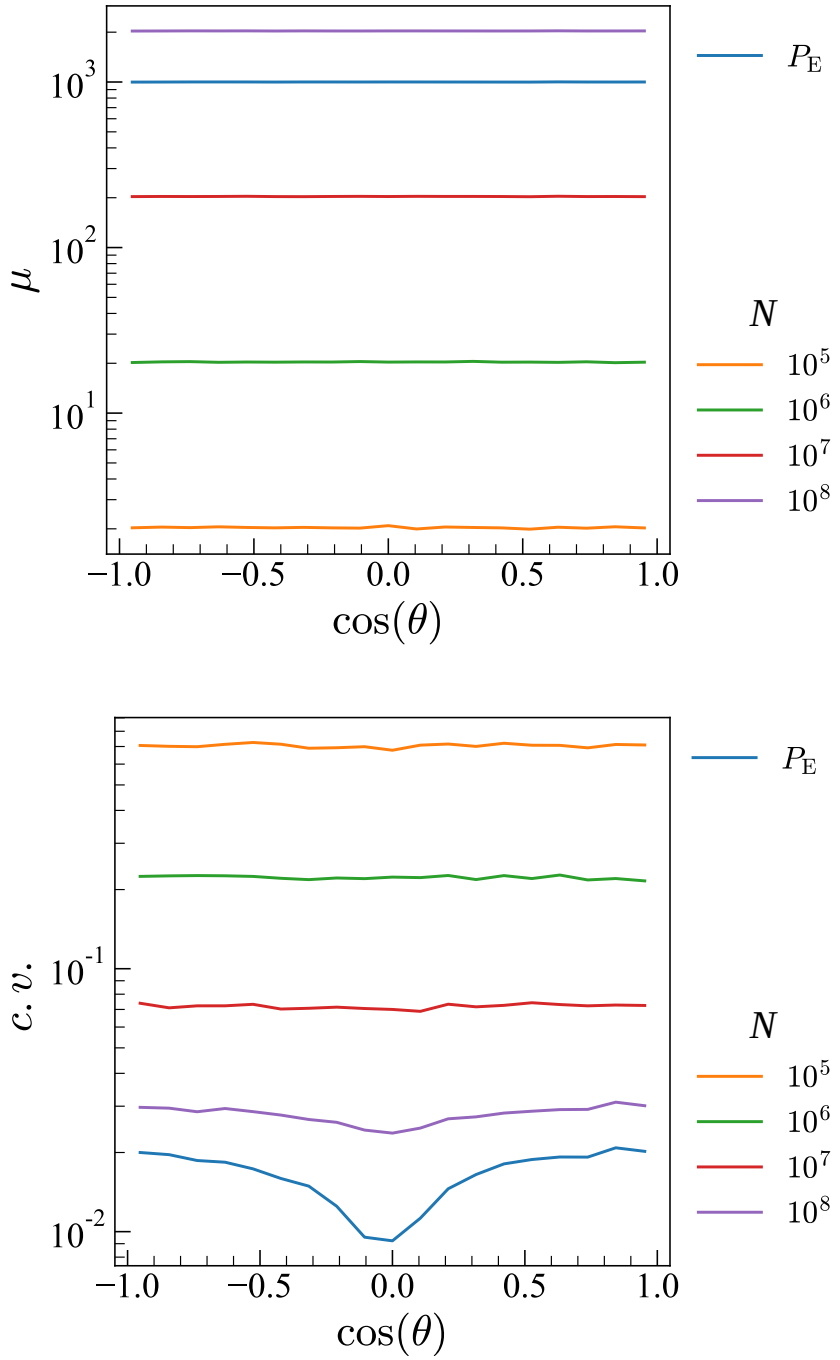

Figure 3.15: The average number of hits (top) and coefficient of variation (bottom) from Equation 3.2 over the galactic latitude. The result of the arrival map P_E is in the blue line.

The results indicate that the average flux displays smoothness across galactic latitudes, as anticipated by Liouville's theorem. However, the anomalous pattern that we see in most of the lensed distribution at higher rigidity, e.g. $R > 10$ EV, results from different levels of fluctuations in each galactic latitude. For some rigidity that

has this structure, e.g. $R = 10$ EV, the bands near the galactic plane have less fluctuation than those near the galactic pole. However, this kind of structure will not be present in the sampled flux map. This is because the fluctuation level is in the lower order of magnitude. The fluctuation in the sampled map is much larger than the probability map it is drawn from; thus, it is not sensitive to this smaller variation. This effect will be observed again if the number of sampled events is higher than the number used to create the incoming distribution. As shown in Figure 3.15, the variation level for $N = 10^5 - 10^7$ is higher than the incoming probability. For $N = 10^8$, only a slight dip at the galactic center appears, like the original distribution.

3.4.2 Angular power spectrum

The anomalous distribution in the lensed map may be inspected using the angular power spectrum:

$$C_l = \frac{1}{2l+1} \sum_{m=-l}^{l} |a_{lm}(R)|^2 . \tag{3.4}$$

where $a_{lm}(R)$ is the coefficient of the spherical harmonics function Y_m^l which is derived from the spherical harmonic transform of the map $P_{\mathrm{G/E}}$:

$$P(R,\theta,\phi) = \sum_{l=0}^{l_{\max}} \sum_{m=-l}^{l} a_{lm}(R)\, Y_l^m(\theta,\phi). \tag{3.5}$$

where (θ, ϕ) is the sperical coordinate. This mathematical tool has the ability to characterize the patterns present in the data on each scale of $4\pi/(l+1)$ steradians.

Here, the lensed distribution of $R = 50$ calculated from the incoming particles $10^3 \times 49152$ is used. The same number of sampled events, $N = 10^5 - 10^8$, is utilized. The results are shown in Figure 3.16, where each spectrum is normalized by its zeroth moment (C_0). The normalized power spectra then have the same monopole moment, which one can easily compare the anisotropic distribution by the relative strength of the other multipole moment.

From the power spectrum in Figure 3.16, these distributions display the isotropic distribution, referred to as the constant value over harmonic moment l [52]. However, the power spectrum for the arrival map has a lower order of magnitude than the sampled flux map, resulting from different numbers of hits in each map. For the set of $N = 10^8$ events, which is larger than the incoming distribution, its power spectrum is roughly at the same level as the arrival distribution. This confirms that the anomalous pattern in the arrival distribution will not be present in the sample distribution, which has a much lower number of events.

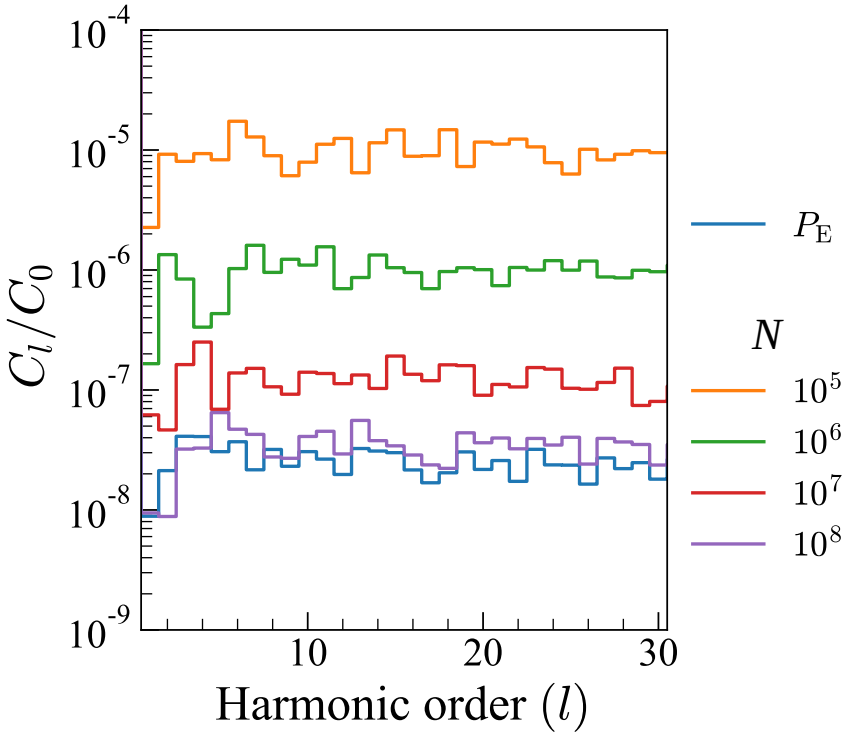

Figure 3.16: Anuglar power spectra for $l \leq 30$ of the arrival probability map (P_{E}), in the blue line, and the resulting simulated event map at a different number of events. The spectra are normalized by their zeroth moment (C_0).

From the analysis in this chapter, it has been demonstrated that the galactic magnetic field accounts for the isotropization: it is not strong enough to create flux anisotropy from the homogeneous source distribution. However, the effect of a single rigidity is only considered, which results in different levels of isotropization for each UHECR species. This suggests that if one would want to modify the spatial distribution or spectral distribution, or both, e.g. a different relative fraction or spectral indices, there could be different species-dependent anisotropy. Thus, the composition anisotropy might be observed.

As an example of another spatial model, the dipolar distribution is introduced. This spatial model is expected from the non-uniform extragalactic source distribution [52]. Apart from the dipole in many contexts, it doesn't say that there is a negative flux in the observation, rather the flux is displayed by the cosine function concerning the direction where the flux is maximum, i.e. the dipolar pole. An example of dipolar distribution with the pole direction at $(l, b) = (240°, 30°)$, with the relative amplitude of the dipole at 10% is presented in the left of Figure 3.17. These initial values are arbitrarily chosen for demonstration.

The lensed distribution on the right of Figure 3.17 exhibits two effects: the change in the dipole amplitude and the relocation of the dipole direction. The relative amplitude is defined by the ratio of the dipole to monopole strength and is computed by fitting the monopole and dipole components using the `healpy.fit_dipole` package. The monopole is simply an average of counts per bin, while the dipole is computed

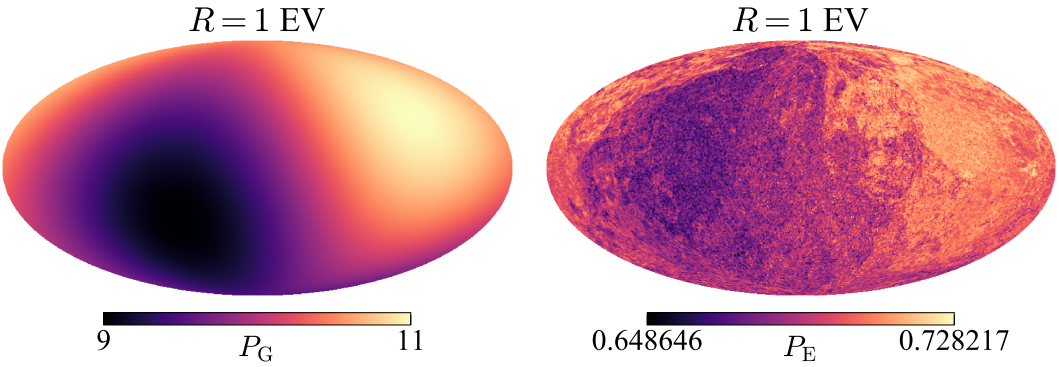

Figure 3.17: Dipolar distribution before (left) and after (right) apply the magnetic lens at $R = 1$ EV.

using linear algebra. For the given dipole amplitude and direction in Figure 3.17, the lensed dipole has a relative amplitude of 2.67%, with the new dipole direction at $(l, b) = (243°, 16°)$, shifted by 0.25 rad.

However, in different dipole directions, the de-amplification and relocation of the dipole are not equal, even for the same rigidity. This is shown in Figure 3.18 where each dipole direction, given by the HEALPix pixelation scheme of order 6, provides different dipole amplitudes and relocation angles α across the entire sky map.

Furthermore, both effects are also rigidity dependent. At low rigidity, i.e. stronger magnetic deflection, there is a correlation between the dipole amplitude and the shift in the dipole direction. For some initial directions that are stronger de-amplified, the shift angle is also large. Nevertheless, this is not found for higher rigidity, even the increase in dipole strength is observed. For the change in direction, this effect decreases along with increasing rigidity. This result demonstrates the complication of introducing a more complex spatial distribution.

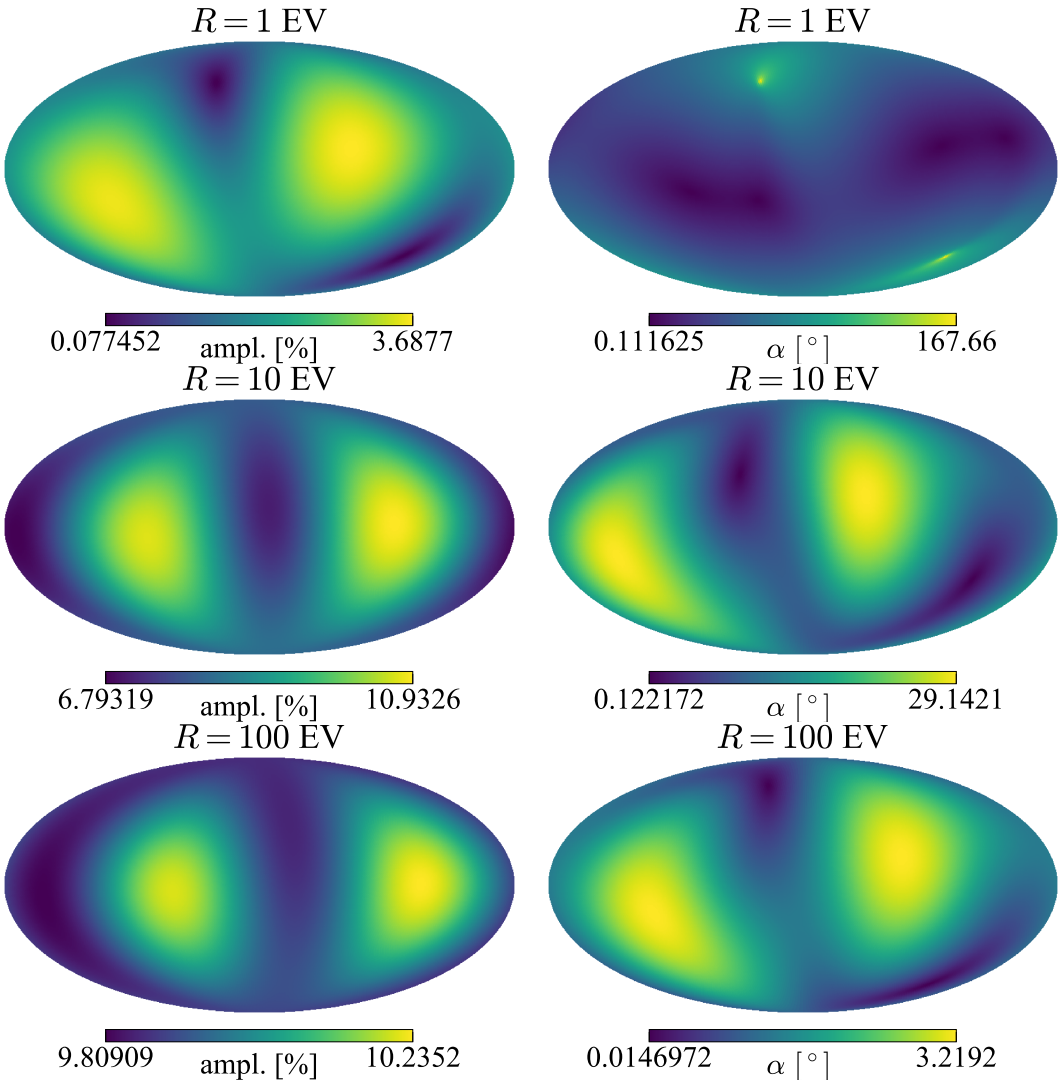

Figure 3.18: Relative dipole amplitude (left column), given in percentage, and angular distance of relocation of the lensed distribution (right column), given in degree, at each dipole direction, computed from the incoming distribution of 10% dipole. From top to bottom is different in rigidity.

Chapter 4

Mass Anisotropy Analysis

The arrival probability distribution from the lensing method directly relates to the average flux distribution over the sky. From this probability map, it is possible to inspect the composition anisotropy, for example, by constructing a fraction map where it is defined as proton flux to the total flux. However, it will be harder to compare the result with the one reported by the Pierre Auger Observatory. So, the event-based analysis will be utilized, where the simulated events are sampled from the arrival distribution. Moreover, to make it more realistic, we need to simulate the measurables as if they were detected.

The primary objective of this chapter is to provide a qualitative analysis of the composition anisotropy in the simulated data by analyzing the mass observable, $X_{\max}$. In the subsequent sections, the method used to simulate the UHECR events based on the arrival distribution will be presented which creates the mock-up measurement reflecting the statistical nature of the cosmic rays. Furthermore, the results for some specific cases are also provided.

4.1 The mass observable distribution

For each event measured by the UHECR experiment, the properties of the primary cosmic ray can be found by analyzing the air shower measurement. This provides the energy, direction, and shower profile. Since the creation of air showers is on stochastic fluctuation, it is impossible to determine which air shower stems from which initial particle. Nevertheless, each primary provides different shower profiles as discussed in Section 2.3.2. From the shower profile, one can extract the maximum atmospheric depth, $X_{\max}$, which is defined as the distance from the atmospheric boundary where the energy of the EAS induced by the cosmic ray is the most dissipated. This parameter becomes the heart of the anisotropy analysis.

In simulations, we can predefine the species, e.g. proton or iron, for each particle from the sampling of the lensed distribution, but the observable of each event is not known. To mimic the complete set of actual measurements, we, therefore, need to randomly assign the $X_{\max}$ parameter according to the particle type and energy. For the straightforward method, we need to simulate an air shower to extract the $X_{\max}$ by fitting the longitudinal profile. This leads to tons of simulations and the fitting

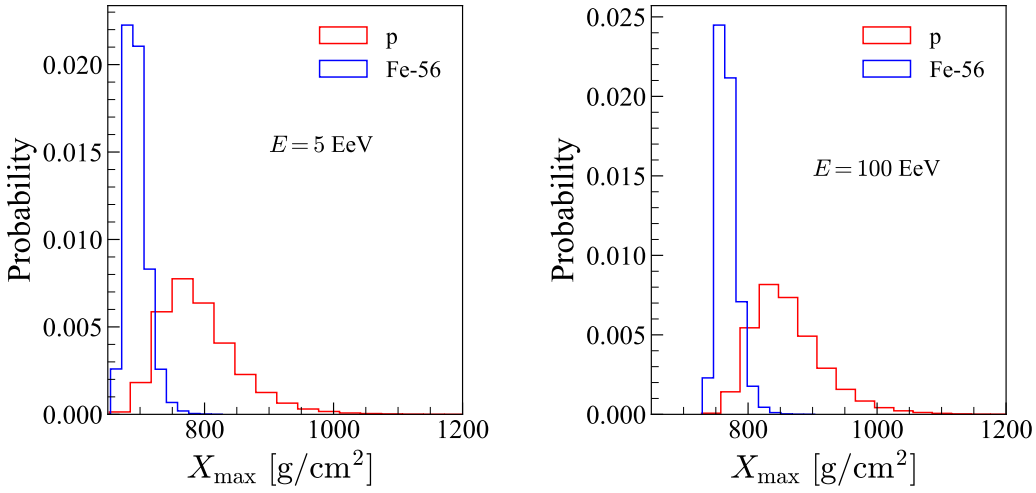

Figure 4.1: Probability distribution of $X_{\max}$ for 5 and 100 EeV proton and iron nucleus. The histograms are calculated by drawing 10^5 $X_{\max}$ each from the generalized Gumble distribution described in [53], with EPOS-LHC interaction model.

of simulated air shower data sets just to get a single value of the observable. As discussed in [53], the value of $X_{\max}$ depends on the convolution of two probability distributions: the point where the shower is initiated and the development of the shower from different energy/primary. However, it is instead reinterpreted using the generalized Gumbel distribution. The parameterization of $X_{\max}$ distribution is derived from the air shower simulations, where different interaction models are being used, and of course, extrapolated.

Therefore, this distribution will be utilized for the production of our simulated $X_{\max}$ data set. This set the advantages for the computational costs. The formulation and the best-fit parameters for this distribution are provided in Appendix D. The examples of the probability distribution of $X_{\max}$ for proton and iron events at $E = 5$ EeV and $E = 100$ EeV are demonstrated in Figure 4.1. One can see the difference in the shape of the distribution of different elements and energies. The mean and standard deviation for each kind as a function of energy is presented in Figure 4.2. For heavy nuclei, the lower value and less fluctuation in $\langle X_{\max} \rangle$ is expected as discussed in Section 2.3.2.

In subsequent applications, it is essential to eliminate the energy dependence from this parameter. To achieve this, [7] introduced an energy-independent parameter,

$$X'_{\max} = X_{\max}(E) - \langle X_{\max} \rangle_{\mathrm{Fe}}(E), \tag{4.1}$$

which will also be used in the analysis.

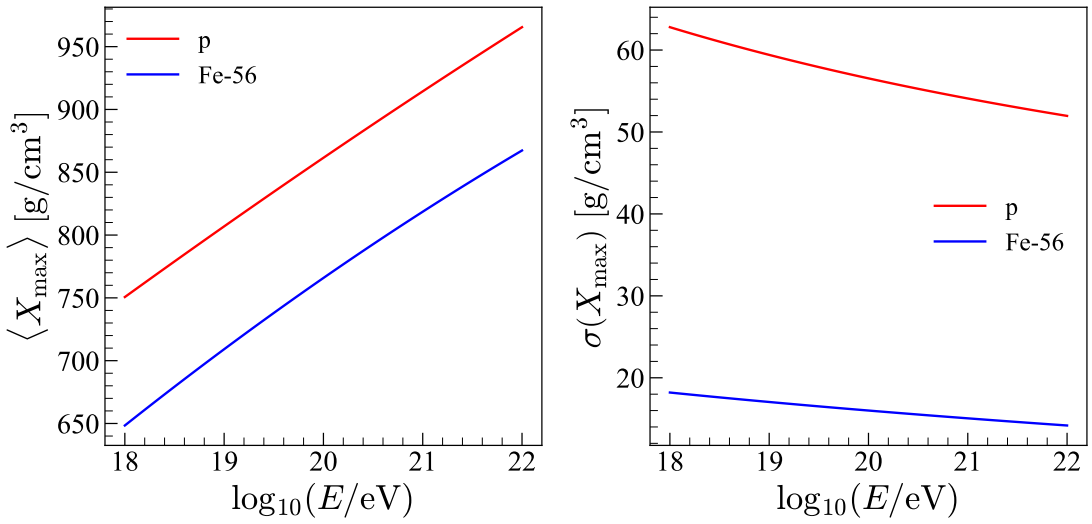

Figure 4.2: The energy dependence of the mean and standard deviation of the $X_{\max}$ distribution in Figure 4.1.

4.2 Simulated observations

As discussed in Section 2, the composition is described through the first and second moments of the $X_{\max}$ distribution. First, the simulated data set is made following the uniform source distribution for the spatial distribution. For the spectral distribution, the exponential cutoff power law function:

$$\frac{\mathrm{d}N}{\mathrm{d}E} = E^{-\gamma} \exp\left(-\frac{E}{Z \cdot R_{\max}}\right). \tag{4.2}$$

is assumed. The energy cut can be explained by the acceleration mechanism of the source. Figure 4.3 shows the energy spectrum for proton and iron. This initial setup is then applied with the lensing matrix to get the observed distribution on Earth.

Next, the simulated events are drawn from the lensed distribution, as demonstrated in Section 3.4. However, by introducing the energy spectrum, the same sampling method is unsuitable as the number of events for each energy should not be predetermined. So instead of drawing the exact number, the author uses the averaged flux map, which is proportional to the observed probability map by a normalization factor, to sample from the Poisson distribution. The total average number of UHECR hits is found by summing all energy bins i and every pixel j. To account for multiple compositions, the contribution factor f_Z is defined such that it satisfies $N_{\mathrm{tot}} = \sum_k N_k$, and

$$N_k = f_k \sum_i \sum_j P_{\mathrm{E}}^k, \tag{4.3}$$

where P_{E}^k is the average arrival flux map of the element k with charge number Z.

The application of the number generator to the average flux map yields a number of simulated events with a total count of around N_{tot}. While each realization may produce a slightly varying total number of simulated events, this variation remains

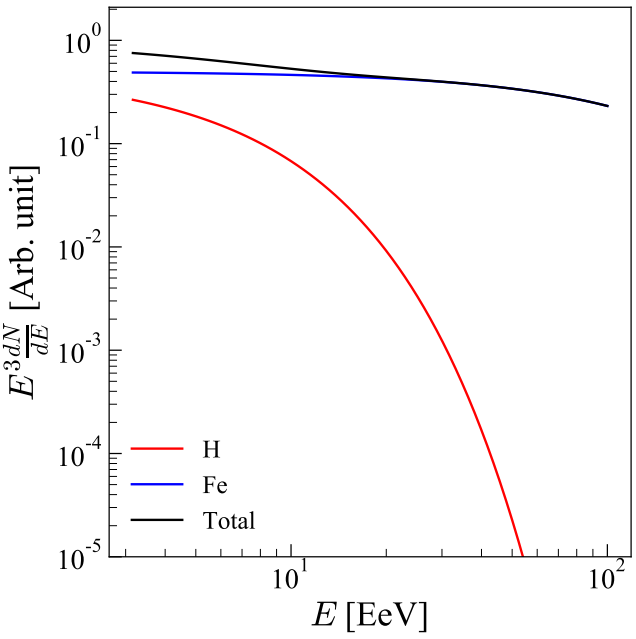

Figure 4.3: UHECR energy spectrum of exponential cut-off power law with $\gamma = 3$ and $R_{\max} = 5$ EV.

relatively small, approximately to the order of $\sqrt{N_{\text{tot}}}$. For example, a total of 50,000 simulated UHECR events will have only 0.4% of the fluctuation in the number of hits per realization.

In each set of simulated datasets, an average of 50,000 arriving UHECRs are generated from the lensed probability map derived from $10^3 \times 49152$ incoming particles with a uniform direction, for both proton and iron. This number is chosen as it is close to the total UHECR counts for $E > 5$ EeV, reported by the Pierre Auger observatory [22]. The equal amount of proton and iron ($f_{\text{p}} = 0.5$) is chosen, and the energy spectrum follows Equation 4.2, with $\gamma = 3$ and $R_{\max} = 5$ EV, spanning a range from $10^{18.5}$ to 10^{20} eV. An illustrative example of the event map is shown in Figure 4.4, with the count map for each energy interval and primary in Figure 4.5.

The bare events in the dataset only contain spatial and spectral information. To incorporate the simulated mass observable measurement, we proceed by randomly assigning the $X_{\max}$ parameter based on the nucleus type and energy of the events. For this purpose, a set of numbers following the Gumbel distribution[1] is drawn using the parameter values provided by [53]. It is important to note that our simulation exclusively considers the EPOS-LHC interaction model.

[1]This is different from the generalized distribution. The parameters are transformed to be able to be used with this number generator. See Appendix D for more details.

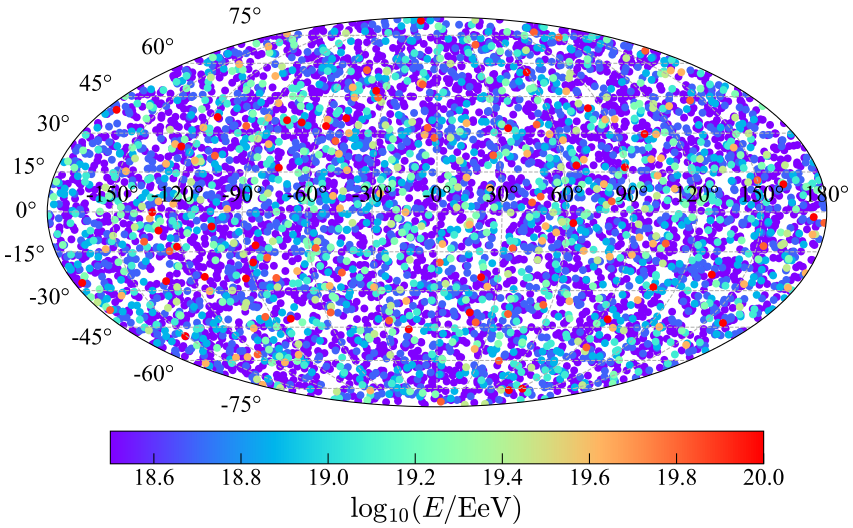

Figure 4.4: A combined event map generated from the isotropic lensed map of the two compositions, following cutoff power-law spectrum. The energy of each event is color-coded.

4.3 The composition map

To illustrate the distinction in mass composition, the procedure presented in Section 6 of [7] is adopted. Considering the direction to be examined, the events are divided using the top-hat function which divides the sky map into two regions. The "in-hat" region comprises events located at an angular distance lower than 30 degrees from the given direction, while events not in this region are considered "out-hat" events. This smoothing function simplifies the analysis of composition by mitigating the complexities arising from the discrete distribution of events.

The test statistics parameter determining the difference in $\langle X_{\max} \rangle$ is then computed from the **Welch's t-test**,

$$t = \frac{\langle X'^{\text{in}}_{\max} \rangle - \langle X'^{\text{out}}_{\max} \rangle}{s_\Delta} \quad , \quad s_\Delta = \sqrt{\frac{\sigma \left(X'^{\text{in}}_{\max} \right)^2}{N_{\text{in}}} + \frac{\sigma \left(X'^{\text{out}}_{\max} \right)^2}{N_{\text{out}}}}, \tag{4.4}$$

where $X'^{\text{in/out}}_{\max}$ is the energy-independent maximum depth in each region. Therefore, the mean of this observable implies a mass composition. The top-hat directions are pixelated according to the HEALPix pixelation of order 4, equivalent to 3072 top-hat directions. The test statistics follow the standard normal distribution, with $\mu = 0$ and $\sigma = 1$[2]. From the composition map in Figure 4.6, heavier composition, in blue shade, means that the region around that direction is observed to have more events with lower $X_{\max}$ compared to the rest of the sky. This is opposite to the lighter composition in the red shade.

To inspect the composition anisotropy, the map of the test statistics in Figure 4.6 shows directly the region where the difference in $\langle X_{\max} \rangle$ is present. If there is a

[2]This estimates from the asymptotic limit of degree of freedom (ν_∞) in t-distribution as the number of events in each region is sufficiently large.

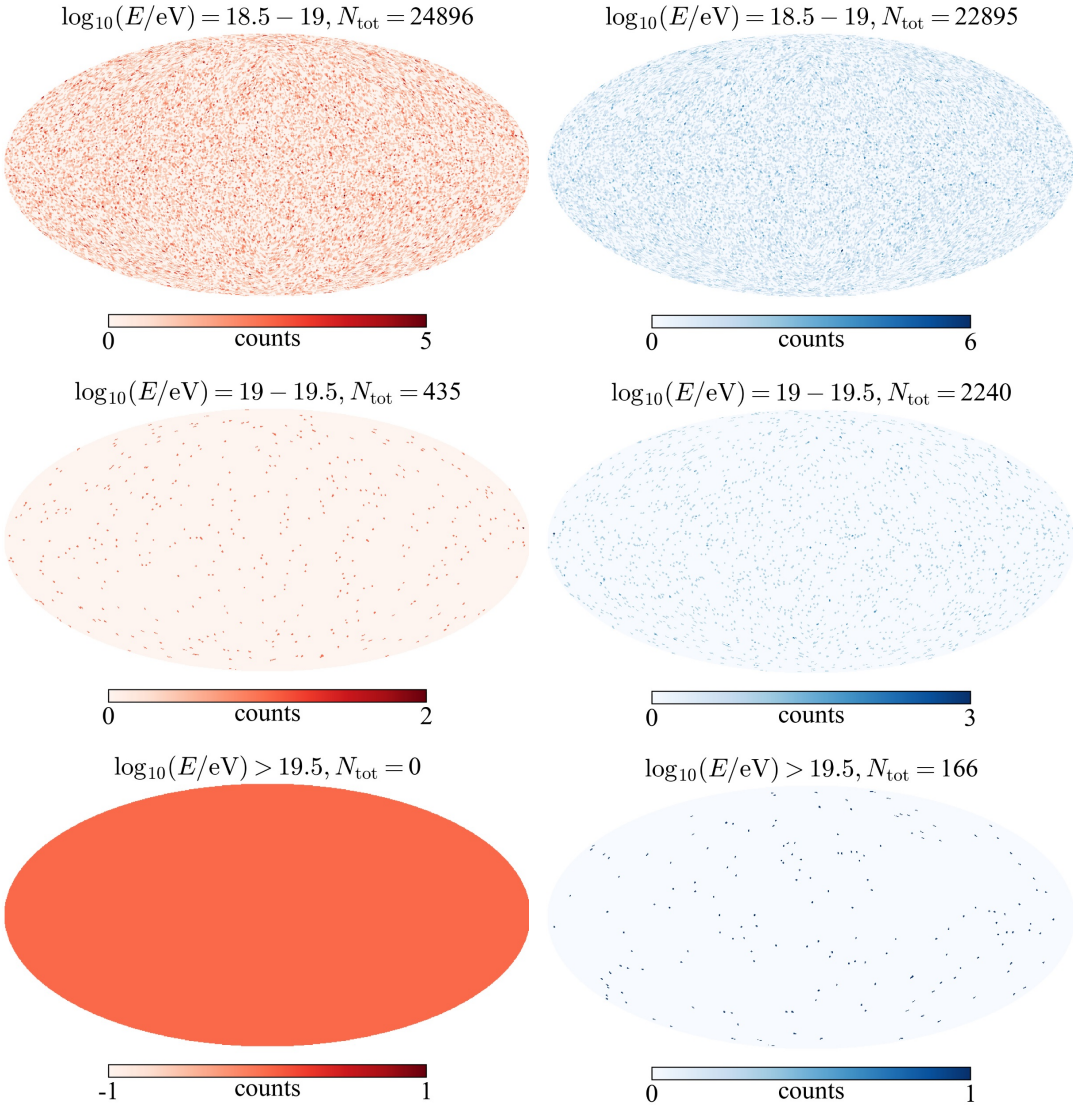

Figure 4.5: The event count map deconstructed at each energy interval, from top row to bottom row. The left and right column is proton and iron events.

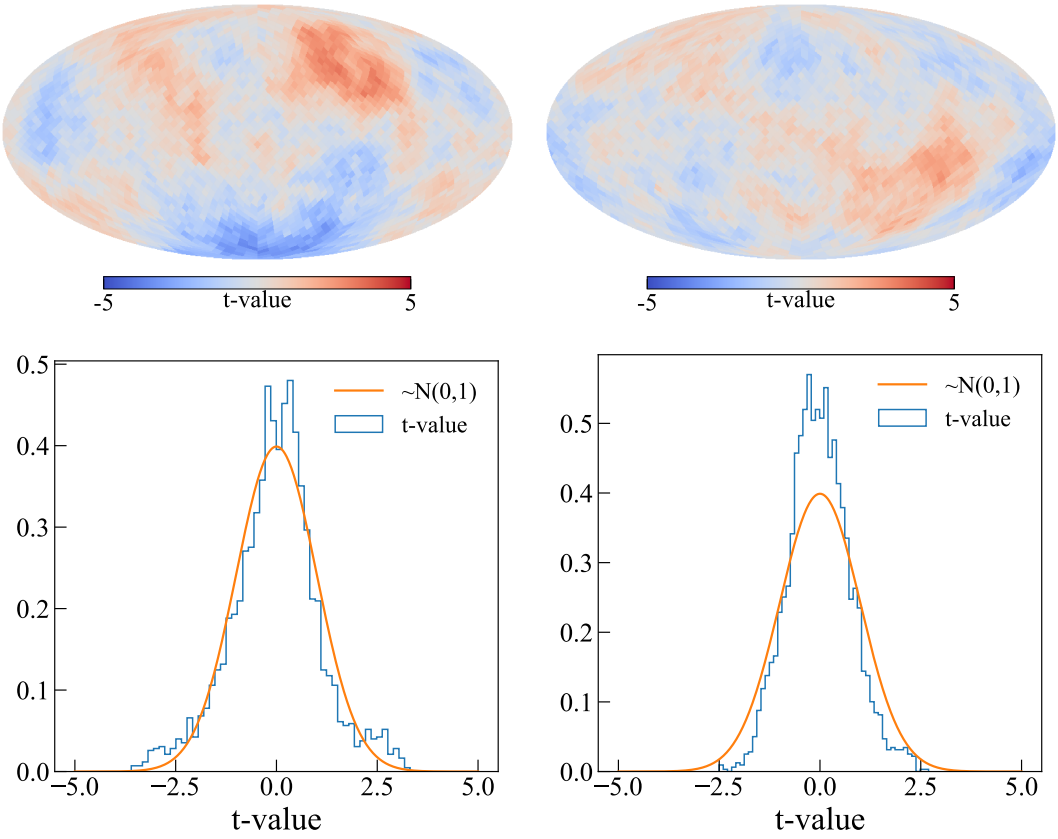

Figure 4.6: Top row: Composition map in t-value of the Welch's test. Bottom row: The histogram of the t-value for the corresponding map. The left and right columns are the different runs of the configuration for the isotropic case.

statistically different composition, the test statistics value is observed to exceed the critical value, either the dark red or dark blue region in the composition map or the value in the histogram.

Upon visual inspection, the histogram does not seem to deviate much from the normal distribution, together with the pale red/blue region in the composition map. The large-scale composition difference as seen in Figure 4.6 can coincidentally occur by randomness, that is, other realizations can have different features as also demonstrated in the same figure. This result qualitatively excludes the hypothesis of the galactic magnetic field being the only influence to induce the observed composition anisotropy.

This is expected as the lensed distribution of isotropic distribution does not provide flux anisotropy, as discussed in Chapter 3. Nevertheless, there are a lot of simplifications in the systematic of the simulation. For example, the spectral function could be different for each primary. Further hypotheses could also be investigated.

4.4 Selected scenarios

4.4.1 Variation in relative component

In this context, we explore scenarios involving varying relative amounts of each primary. The test for two scenarios is chosen: a lower proton fraction ($f_{\mathrm{p}} = 0.25$) and a higher proton fraction ($f_{\mathrm{p}} = 0.75$). Apart from the proton fraction, the simulations are configured the same as in the equal fraction case. The results are presented in Figure 4.7.

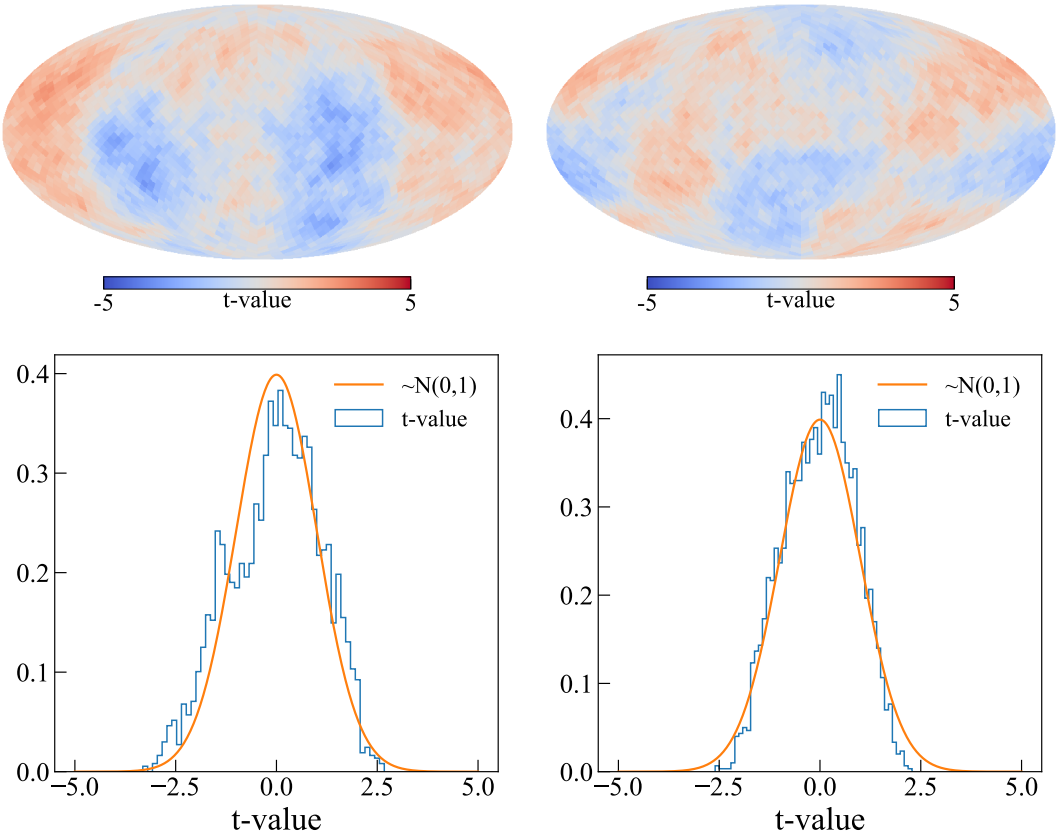

Figure 4.7: The results for $f_p = 0.25$ (left) and $f_p = 0.75$ (right) with the same labels as Figure 4.6

The results are also not particularly different from the equal fraction for both cases. Thus, the change in fraction would also not be the case for the composition anisotropy.

4.4.2 Dipolar distribution

It is demonstrated in [52] that the extragalactic source with non-uniform distribution could induce a dipolar distribution at the edge of the galaxy. Therefore, the author would like to test the method with the dipolar incoming distribution. The

investigation for the deflection of the magnetic field to the dipole direction and the dipolar strength is already presented at the end of Chapter 3.

As per the demonstration, the author initially selects the dipole to have the maximum amplitude at $(l, b) = (240°, 30°)$, with 10% amplitude. This direction is close to where it is suggested from the study of the original dipole direction before magnetic deflection of observed UHECR flux from the Pierre Auger Observatory result [6]. This specific spatial distribution is applied for both proton and iron. The simulation follows the same spectral distribution as in the previous section, with $N_{\text{tot}} = 50,000$ and $f_p = 0.50$.

The composition map in Figure 4.8 presents a stronger deviation from the normal distribution, compared to the isotropic case. However, the value of test statistics is not strong enough to confirm the composition anisotropy.

This result suggests that this spatial function could be the reason for composition anisotropy. However, further analysis could be made, e.g. different dipole direction for each primary, or different dipole amplitude.

With the analysis framework provided in this chapter, it is shown that the galactic magnetic field is an important factor for the UHECR simulation. However, it is also confirmed that the spatial distribution of the source provides a stronger effect on the observed UHECR.

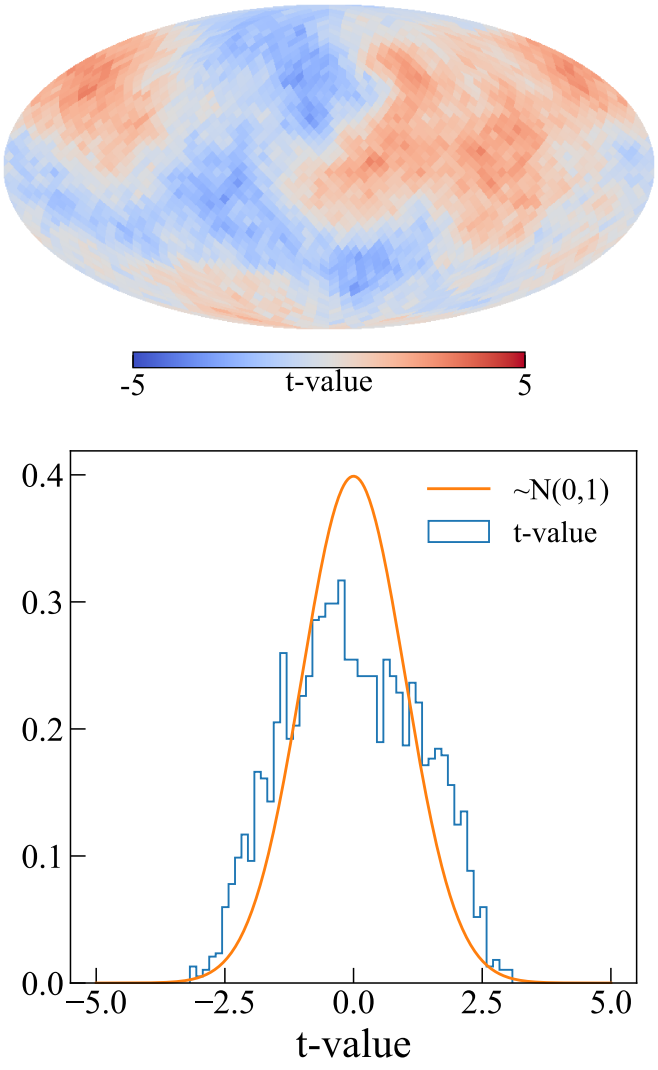

Figure 4.8: Composition map for the dipolar distribution for incoming UHECR.

Chapter 5

Conclusion and Outlook

The UHECR composition anisotropy is one of the keys to constrain the origin of UHECR. In this thesis, the simulation using the lensing method is presented to qualitatively assess the composition anisotropy of UHECR. The effect of the galactic magnetic field is investigated for the uniform distribution of different nuclei at each energy. A simple framework to mimic UHECR measurements has been proposed. This method has been applied to test some assumptions of the UHECR entering the galaxy.

In the implementation of galactic magnetic lensing, it is demonstrated that the GMF contributes to isotropization, even though there are higher flux fluctuations along the galactic latitude. The fluctuation presented in the spatial distribution of arrival distribution will not pose on the measurement at Earth due to lower statistics. This isotropization effect is stronger for cosmic rays with higher charge numbers at the same energy. Consequently, for heavy nuclei, the former distribution is much affected at low energy, while it is preserved at high energy. This implies the spectral dependence on the observed anisotropy. Further inspection is made on the dipolar incoming distribution. This suggests a more potential distribution, as it can be isotropized at low rigidity while keeping the dipolar flux in high energy. However, the effect is also directional-dependent for the dipole. This makes it harder to constrain the potential extragalactic source that can induce the dipolar distribution at the edge of the galaxy.

The composition analysis presented here includes all-sky maps; however, there is an obvious difference in acceptance of the detector at each declination. Thus, the event selection criteria are not applied. This is not included in the analysis routine, though it might lead to a difference between the result obtained from this method and the actual observation. This could be further investigated in future work, e.g., by combining the results from the northern and southern hemispheres to cover the whole sky.

In conclusion, the analysis of this thesis excludes magnetic deflection as the only factor that creates composition-dependent anisotropy. Aspects of the extragalactic factors, e.g. extragalactic source distribution, are promising for future research.

Appendix A

Energy loss due to magnetic field

The loss mechanism in magnetic deflection is synchrotron radiation. The average synchrotron power for a charged particle with mass m is computed using the formula [54]:

$$\left\langle \frac{dE}{dt} \right\rangle = \frac{4}{3} c \sigma_{\mathrm{T}} \left(\frac{m_e}{m} \right)^2 \gamma^2 \beta^2 u_B \tag{A.1}$$

where m_e is the electron mass, $\sigma_{\mathrm{T}} = 6.65 \times 10^{-25}$ cm^2 is the Thomson cross-section, $\gamma := 1/\sqrt{1-\beta^2}$ is the Lorentz factor, and $u_B := B^2/8\pi$ is the magnetic energy density. The value is given in the cgs unit system.

For a 1 EeV proton moving through the uniform magnetic field of 6 μG, the typical value for the Milky Way's magnetic field, the radiation power is approximately 10^{-14} erg/s. Consider this proton travelling within the galaxy for 100 kpc, equivalent to the time spent of 10^{10} s, the total energy loss is only 10^{-8} EeV. This is relatively tiny compared to its initial energy; thus, one does not need to consider the energy loss in magnetic lensing.

Appendix B

Arrival probability over galactic latitude

Here, the numerical values of the two-dimensional probability distribution in Figure 3.13 are presented in Table B.1, B.2, and B.3 for $R = 1, 10, 100$ EV, respectively. The average galactic latitude ($\overline{b}$) represents the galactic latitude for the corresponding band, which is not equally spaced due to the pixelated scheme. The table runs the same as the figure: each column means the galactic latitude band for the incoming distribution (b_{G}), while each row is for the arrival distribution (b_E).

$\bar{b}_E/\bar{b}_G$ [°]	-72.3	-57.5	-47.5	-39.2	-31.8	-24.9	-18.4	-12.2	-6.0	0.0	6.0	12.2	18.4	24.9	31.8	39.2	47.5	57.5	72.3
72.3	0.003	0.004	0.005	0.005	0.004	0.005	0.009	0.020	0.052	0.118	0.227	0.355	0.501	0.650	0.723	0.725	0.699	0.485	0.286
57.5	0.003	0.003	0.003	0.003	0.003	0.004	0.007	0.016	0.039	0.088	0.172	0.289	0.448	0.620	0.777	0.851	0.867	0.622	0.377
47.5	0.002	0.002	0.003	0.003	0.003	0.003	0.006	0.013	0.036	0.079	0.161	0.271	0.418	0.630	0.808	0.856	0.931	0.704	0.389
39.2	0.002	0.002	0.002	0.003	0.003	0.003	0.006	0.014	0.035	0.078	0.150	0.259	0.386	0.594	0.781	0.913	1.027	0.735	0.388
31.8	0.002	0.002	0.002	0.003	0.003	0.003	0.005	0.013	0.033	0.073	0.152	0.242	0.390	0.587	0.774	0.907	1.026	0.774	0.419
24.9	0.002	0.002	0.002	0.003	0.003	0.003	0.006	0.013	0.033	0.076	0.150	0.241	0.389	0.607	0.762	0.893	0.991	0.773	0.426
18.4	0.002	0.002	0.003	0.003	0.003	0.003	0.006	0.014	0.035	0.075	0.152	0.258	0.405	0.602	0.770	0.917	0.997	0.741	0.373
12.2	0.002	0.003	0.003	0.003	0.003	0.004	0.006	0.015	0.037	0.074	0.157	0.254	0.414	0.618	0.812	0.911	0.996	0.722	0.339
6.0	0.002	0.002	0.002	0.002	0.003	0.003	0.007	0.016	0.033	0.077	0.156	0.259	0.414	0.625	0.825	0.923	0.984	0.700	0.351
0.0	0.002	0.002	0.002	0.002	0.003	0.003	0.006	0.014	0.036	0.077	0.151	0.244	0.417	0.659	0.843	0.946	0.991	0.698	0.325
-6.0	0.002	0.002	0.003	0.002	0.003	0.003	0.007	0.015	0.036	0.075	0.159	0.254	0.429	0.663	0.850	0.937	1.010	0.663	0.302
-12.2	0.002	0.002	0.003	0.002	0.003	0.004	0.007	0.016	0.039	0.081	0.163	0.261	0.464	0.684	0.880	0.947	0.955	0.600	0.251
-18.4	0.002	0.003	0.003	0.003	0.003	0.004	0.007	0.016	0.039	0.086	0.173	0.285	0.466	0.708	0.880	0.943	0.924	0.559	0.227
-24.9	0.003	0.002	0.003	0.003	0.003	0.004	0.008	0.016	0.041	0.087	0.175	0.282	0.479	0.703	0.848	0.925	0.896	0.558	0.242
-31.8	0.002	0.003	0.003	0.003	0.003	0.004	0.007	0.019	0.037	0.085	0.171	0.291	0.475	0.726	0.867	0.922	0.888	0.547	0.223
-39.2	0.002	0.003	0.004	0.003	0.004	0.004	0.008	0.018	0.041	0.090	0.178	0.298	0.488	0.695	0.853	0.893	0.870	0.548	0.228
-47.5	0.002	0.003	0.004	0.004	0.004	0.005	0.008	0.019	0.043	0.094	0.189	0.304	0.488	0.710	0.818	0.851	0.839	0.542	0.234
-57.5	0.003	0.004	0.004	0.005	0.005	0.006	0.010	0.024	0.049	0.108	0.200	0.317	0.471	0.627	0.749	0.782	0.793	0.547	0.258
-72.3	0.003	0.004	0.004	0.005	0.006	0.007	0.011	0.024	0.050	0.103	0.204	0.324	0.463	0.611	0.742	0.771	0.773	0.537	0.260

$\times 10^{-2}$

Table B.1: Arrival probability as presented in Figure 3.13 for $R = 1$ EV.

$\bar{b}_E/\bar{b}_G$ [°]	-72.3	-57.5	-47.5	-39.2	-31.8	-24.9	-18.4	-12.2	-6.0	0.0	6.0	12.2	18.4	24.9	31.8	39.2	47.5	57.5	72.3
72.3	0.000	0.000	0.000	0.000	0.000	0.000	0.000	0.000	0.000	0.000	0.000	0.000	0.000	0.000	0.000	0.001	0.345	1.693	3.065
57.5	0.000	0.000	0.000	0.000	0.000	0.000	0.000	0.000	0.000	0.000	0.000	0.000	0.000	0.000	0.126	0.445	1.380	1.945	1.109
47.5	0.000	0.000	0.000	0.000	0.000	0.000	0.000	0.000	0.000	0.000	0.000	0.000	0.024	0.361	0.725	0.841	1.556	1.112	0.576
39.2	0.000	0.000	0.000	0.000	0.000	0.000	0.000	0.000	0.000	0.000	0.000	0.110	0.600	0.742	0.909	1.540	0.878	0.375	0.469
31.8	0.000	0.000	0.000	0.000	0.000	0.000	0.000	0.000	0.000	0.004	0.090	0.369	1.025	0.914	1.829	0.992	0.375	0.208	0.291
24.9	0.000	0.000	0.000	0.000	0.000	0.001	0.002	0.018	0.068	0.172	0.378	0.646	0.879	2.122	1.238	0.371	0.265	0.218	0.086
18.4	0.000	0.000	0.000	0.000	0.000	0.005	0.019	0.056	0.177	0.334	0.475	0.675	1.658	2.072	0.531	0.317	0.150	0.095	0.023
12.2	0.000	0.000	0.000	0.000	0.001	0.009	0.044	0.111	0.212	0.313	0.545	1.293	2.173	1.389	0.339	0.160	0.069	0.031	0.008
6.0	0.000	0.000	0.000	0.000	0.000	0.006	0.038	0.113	0.184	0.321	0.742	1.699	2.034	1.023	0.304	0.111	0.068	0.041	0.013
0.0	0.000	0.001	0.002	0.003	0.005	0.012	0.044	0.118	0.198	0.316	0.653	1.409	1.888	1.327	0.470	0.099	0.033	0.035	0.013
-6.0	0.000	0.009	0.032	0.037	0.038	0.040	0.072	0.185	0.272	0.341	0.593	1.091	1.461	1.191	0.539	0.164	0.020	0.002	0.000
-12.2	0.005	0.037	0.071	0.056	0.043	0.054	0.084	0.216	0.424	0.516	0.727	1.053	1.011	0.734	0.383	0.150	0.022	0.000	0.000
-18.4	0.015	0.100	0.109	0.084	0.068	0.064	0.091	0.206	0.457	0.565	0.844	1.166	0.864	0.417	0.178	0.054	0.005	0.000	0.000
-24.9	0.117	0.138	0.138	0.104	0.079	0.049	0.049	0.108	0.280	0.513	1.080	1.600	0.929	0.222	0.027	0.004	0.000	0.000	0.000
-31.8	0.277	0.179	0.104	0.143	0.087	0.072	0.066	0.189	0.328	0.618	1.094	1.272	0.366	0.057	0.003	0.000	0.000	0.000	0.000
-39.2	0.337	0.221	0.179	0.142	0.134	0.114	0.142	0.395	0.774	0.595	0.467	0.235	0.030	0.001	0.000	0.000	0.000	0.000	0.000
-47.5	0.569	0.182	0.202	0.136	0.169	0.181	0.422	0.674	0.409	0.104	0.029	0.004	0.000	0.000	0.000	0.000	0.000	0.000	0.000
-57.5	0.813	0.276	0.304	0.273	0.335	0.395	0.303	0.079	0.002	0.000	0.000	0.000	0.000	0.000	0.000	0.000	0.000	0.000	0.000
-72.3	1.022	0.615	0.741	0.466	0.151	0.023	0.001	0.000	0.000	0.000	0.000	0.000	0.000	0.000	0.000	0.000	0.000	0.000	0.000

$\times 10^{-2}$

Table B.2: Arrival probability as presented in Figure 3.13 for $R = 10$ EV.

$\bar{b}_E/\bar{b}_G$ [°]	-72.3	-57.5	-47.5	-39.2	-31.8	-24.9	-18.4	-12.2	-6.0	0.0	6.0	12.2	18.4	24.9	31.8	39.2	47.5	57.5	72.3
72.3	0.000	0.000	0.000	0.000	0.000	0.000	0.000	0.000	0.000	0.000	0.000	0.000	0.000	0.000	0.000	0.000	0.000	0.178	5.160
57.5	0.000	0.000	0.000	0.000	0.000	0.000	0.000	0.000	0.000	0.000	0.000	0.000	0.000	0.000	0.000	0.000	0.226	4.601	0.367
47.5	0.000	0.000	0.000	0.000	0.000	0.000	0.000	0.000	0.000	0.000	0.000	0.000	0.000	0.000	0.000	0.248	4.540	0.412	0.000
39.2	0.000	0.000	0.000	0.000	0.000	0.000	0.000	0.000	0.000	0.000	0.000	0.000	0.000	0.000	0.311	4.379	0.475	0.000	0.000
31.8	0.000	0.000	0.000	0.000	0.000	0.000	0.000	0.000	0.000	0.000	0.000	0.000	0.000	0.315	4.393	0.486	0.000	0.000	0.000
24.9	0.000	0.000	0.000	0.000	0.000	0.000	0.000	0.000	0.000	0.000	0.000	0.000	0.408	4.191	0.525	0.000	0.000	0.000	0.000
18.4	0.000	0.000	0.000	0.000	0.000	0.000	0.000	0.000	0.000	0.000	0.000	0.395	4.284	0.542	0.000	0.000	0.000	0.000	0.000
12.2	0.000	0.000	0.000	0.000	0.000	0.000	0.000	0.000	0.000	0.000	0.593	4.087	0.607	0.000	0.000	0.000	0.000	0.000	0.000
6.0	0.000	0.000	0.000	0.000	0.000	0.000	0.000	0.000	0.009	0.981	4.068	0.835	0.000	0.000	0.000	0.000	0.000	0.000	0.000
0.0	0.000	0.000	0.000	0.000	0.000	0.000	0.000	0.000	0.107	5.686	1.345	0.001	0.000	0.000	0.000	0.000	0.000	0.000	0.000
-6.0	0.000	0.000	0.000	0.000	0.000	0.000	0.000	0.024	1.684	4.638	0.247	0.000	0.000	0.000	0.000	0.000	0.000	0.000	0.000
-12.2	0.000	0.000	0.000	0.000	0.000	0.000	0.075	1.947	2.702	0.058	0.000	0.000	0.000	0.000	0.000	0.000	0.000	0.000	0.000
-18.4	0.000	0.000	0.000	0.000	0.000	0.179	2.266	2.186	0.003	0.000	0.000	0.000	0.000	0.000	0.000	0.000	0.000	0.000	0.000
-24.9	0.000	0.000	0.000	0.000	0.287	2.597	1.802	0.000	0.000	0.000	0.000	0.000	0.000	0.000	0.000	0.000	0.000	0.000	0.000
-31.8	0.000	0.000	0.000	0.385	2.862	1.500	0.000	0.000	0.000	0.000	0.000	0.000	0.000	0.000	0.000	0.000	0.000	0.000	0.000
-39.2	0.000	0.000	0.369	3.300	1.223	0.000	0.000	0.000	0.000	0.000	0.000	0.000	0.000	0.000	0.000	0.000	0.000	0.000	0.000
-47.5	0.000	0.405	3.540	0.992	0.000	0.000	0.000	0.000	0.000	0.000	0.000	0.000	0.000	0.000	0.000	0.000	0.000	0.000	0.000
-57.5	0.328	3.849	0.764	0.000	0.000	0.000	0.000	0.000	0.000	0.000	0.000	0.000	0.000	0.000	0.000	0.000	0.000	0.000	0.000
-72.3	4.576	0.454	0.000	0.000	0.000	0.000	0.000	0.000	0.000	0.000	0.000	0.000	0.000	0.000	0.000	0.000	0.000	0.000	0.000

$\times 10^{-2}$

Table B.3: Arrival probability as presented in Figure 3.13 for $R = 100$ EV.

Appendix C

Effectiveness parameter for different number of initial particles

The total number of UHECR entering the vicinity of the galaxy is not easily determined. One can choose this to be as large as possible, but this is not realized based on the computational resource. However, the difference in initial numbers induces the different values of magnetic effectiveness discussed in the text. To address this, some initial numbers of UHECR are chosen to test the consistency of the effectiveness parameter.

Here, the effectiveness parameter is computed for $f = 10^2, 10^3, 10^4$, and $R = 1, 10, 100$ EV. Figure C.1 shows the evolution of the parameter over the initial number, where the value is observed to be consistent at $f > 10^4$. So, the simulation stops at this value. Figure C.2 and C.3 show the histogram of flux distribution for $f = 1$ and $f = 100$, respectively.

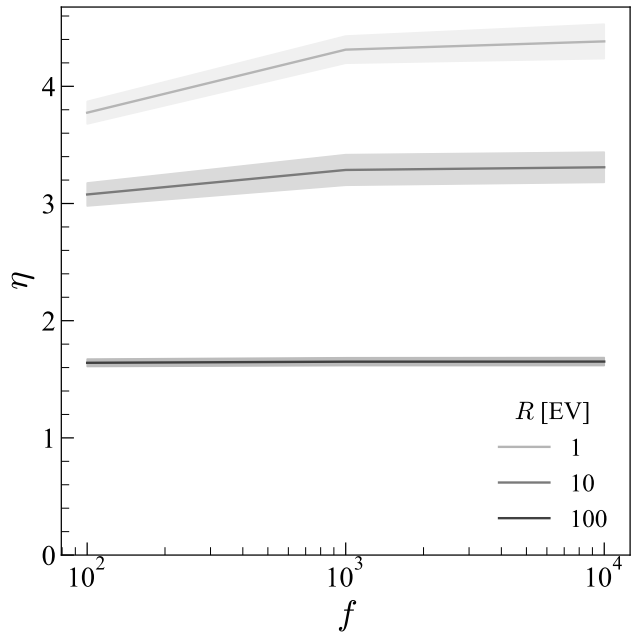

Figure C.1: Effectiveness parameter over different initial numbers of particle $f \times 49152$.

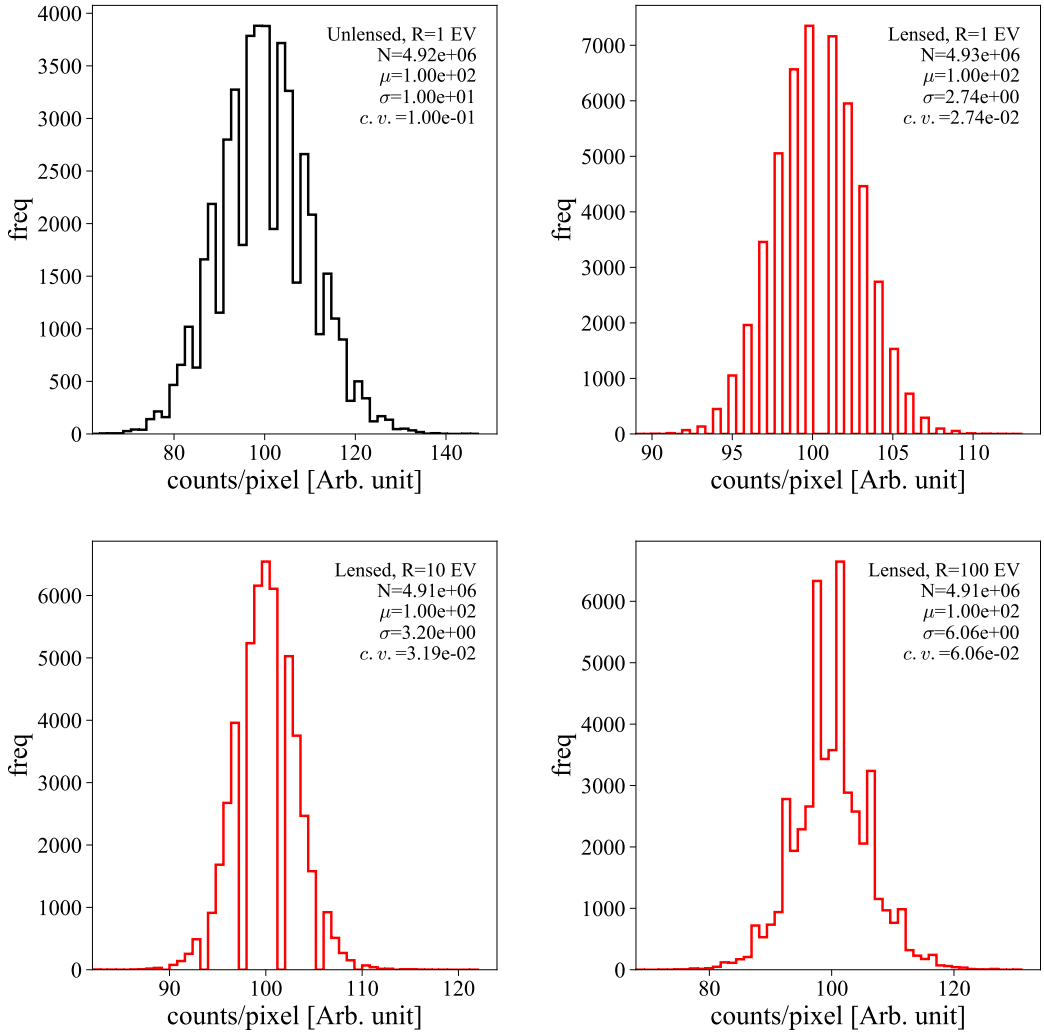

Figure C.2: Histograms of the flux distribution with $f = 10^2$ before (top left) and after applying the magnetic lens at $R = 1,\ 10,$ and 100 EV.

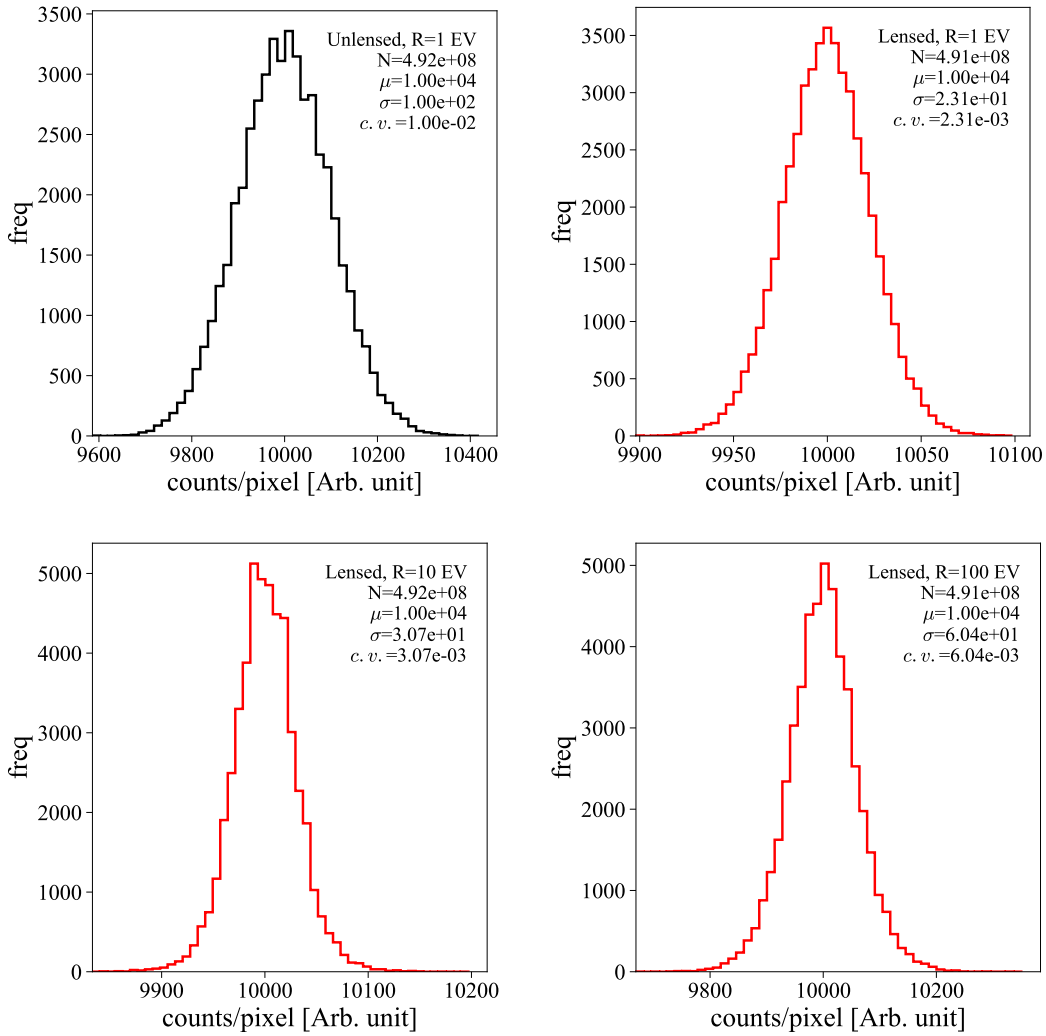

Figure C.3: Histograms of the flux distribution with $f = 10^4$ before (top left) and after applying the magnetic lens at $R = 1,\ 10,$ and 100 EV.

Appendix D

Description of the generalized Gumbel distribution

D.1 Parametrization

The generalized Gumbel distribution is given by [53]:

$$\mathcal{G}(x;\mu,\sigma,\lambda) = \frac{1}{\sigma}\frac{\lambda^{\lambda}}{\Gamma(\lambda)}\left(\lambda z - \lambda e^{-z}\right), \quad z = \frac{x-\mu}{\sigma} \tag{D.1}$$

where the shape parameters (μ, σ, λ) depend on the mass number A and energy E of the cosmic ray. They are parameterized using an empirical polynomial function:

$$\mu(A,E) = p_0^{\mu} + p_1^{\mu}\log_{10}(E/E_0) + p_2^{\mu}\log_{10}^2(E/E_0) \tag{D.2}$$
$$\sigma(A,E) = p_0^{\sigma} + p_1^{\sigma}\log_{10}(E/E_0) \tag{D.3}$$
$$\lambda(A,E) = p_0^{\lambda} + p_1^{\lambda}\log_{10}(E/E_0) \tag{D.4}$$

where $E_0 = 10^{19}$ EeV. Each coefficient is parametrized using another empirical function:

$$p_0^{\mu,\sigma,\lambda} = a_0^{\mu,\sigma,\lambda} + a_1^{\mu,\sigma,\lambda}\ln(A) + a_2^{\mu,\sigma,\lambda}\ln^2(A) \tag{D.5}$$
$$p_1^{\mu,\sigma,\lambda} = b_0^{\mu,\sigma,\lambda} + b_1^{\mu,\sigma,\lambda}\ln(A) + b_2^{\mu,\sigma,\lambda}\ln^2(A) \tag{D.6}$$
$$p_2^{\mu} = c_0^{\mu} + c_1^{\mu}\ln(A) + c_2^{\mu}\ln^2(A). \tag{D.7}$$

In total, there are 21 free parameters. The best-fit parameters for the EPOS-LHC interaction model are presented in Table D.1.

EPOS-LHC	a_0	a_1	a_2	b_0	b_1	b_2
μ	774.647	-7.659	-2.385	57.943	-0.810	0.273
σ	30.727	12.734	-2.953	0.371	-1.516	0.300
λ	0.590	0.691	0.069	0.046	0.038	0.007

EPOS-LHC	c_0	c_1	c_2
μ	-1.029	-0.157	-0.022

Table D.1: Fitted parameters of the distribution of $X_{\max}$ using EPOS-LHC interaction model (taken from [53]).

D.2 Transformation of shape parameter

As derived in Appendix A of [53], the mean and standard deviation of the generalized Gumbel distribution can be solved analytically,

$$\tilde{\mu} = \mu_{\mathcal{G}} + \sigma \ln \lambda_{\mathcal{G}} - \sigma\psi(\lambda_{\mathcal{G}}) \tag{D.8}$$

$$\tilde{\sigma} = \sigma_{\mathcal{G}}\psi'(\lambda_{\mathcal{G}}), \tag{D.9}$$

where $\psi^{(n)}$ is the polygamma function, defined as the n^{th} derivative of $\ln\Gamma(z)$. This relates to the shape parameter of the ordinary Gumbel distribution,

$$g(x;\mu,\sigma) = \frac{1}{\sigma}\exp\left[-z - \exp\left(-z\right)\right], \quad z = \frac{x-\mu}{\sigma}, \tag{D.10}$$

by

$$\mu_g = \tilde{\mu} - \gamma\sigma, \tag{D.11}$$

$$\sigma_g = \frac{\sqrt{6}}{\pi}\tilde{\sigma}. \tag{D.12}$$

where $\gamma = 0.57721$. This shape parameter can then be used with the random number generator of Gumbel distribution via the Python package `np.random.gumbel`.

Bibliography

[1] V. F. Hess, "Über Beobachtungen der durchdringenden Strahlung bei sieben Freiballonfahrten," *Physikalische Zeitschrift*, vol. 13, pp. 1084–1091, 1912.

[2] R. A. Millikan and G. H. Cameron, "The origin of the cosmic rays," *Physical Review*, vol. 32, pp. 533–557, 4 Oct. 1928.

[3] The Pierre Auger Collaboration, "The pierre auger cosmic ray observatory," *Nuclear Instruments and Methods in Physics Research Section A: Accelerators, Spectrometers, Detectors and Associated Equipment*, vol. 798, pp. 172–213, 2015, ISSN: 0168-9002.

[4] R. Abbasi *et al.*, "Telescope Array Radar (TARA) observatory for Ultra-High Energy Cosmic Rays," *Nuclear Instruments and Methods in Physics Research A*, vol. 767, pp. 322–338, Dec. 2014. arXiv: 1405.0057 [astro-ph.IM].

[5] CMS Collaboration, "First measurement of the top quark pair production cross section in proton-proton collisions at $\sqrt{s} = 13.6$ TeV," *arXiv e-prints*, arXiv:2303.10680, arXiv:2303.10680, Mar. 2023. arXiv: 2303.10680 [hep-ex].

[6] The Pierre Auger Collaboration *et al.*, "Observation of a large-scale anisotropy in the arrival directions of cosmic rays above 8×10^{18} ev," *Science*, vol. 357, no. 6357, pp. 1266–1270, 2017.

[7] E. Mayotte and T. Fitoussi, "Update on the indication of a mass-dependent anisotropy above $10^{18.7}$ ev in the hybrid data of the pierre auger observatory," *EPJ web of conferences*, vol. 283, p. 03 003, 2023.

[8] G. Benford and R. Protheroe, "Fossil agn jets as ultrahigh-energy particle accelerators," *Monthly Notices of the Royal Astronomical Society*, vol. 383, no. 2, pp. 663–672, 2008.

[9] A. Haungs *et al.*, "Energy spectrum and mass composition of high-energy cosmic rays," *Reports on Progress in Physics*, vol. 66, no. 7, p. 1145, Jun. 2003.

[10] W. Heitler, *The quantum theory of radiation* (International Series of Monographs on Physics). Oxford: Oxford University Press, 1936, vol. 5.

[11] J. Matthews, "A Heitler model of extensive air showers," *Astroparticle Physics*, vol. 22, pp. 387–397, 2005.

[12] T. K. Gaisser and A. M. Hillas, "Reliability of the Method of Constant Intensity Cuts for Reconstructing the Average Development of Vertical Showers," in *International Cosmic Ray Conference*, ser. International Cosmic Ray Conference, vol. 8, Jan. 1977, p. 353.

[13] K. Kamata and J. Nishimura, "The Lateral and the Angular Structure Functions of Electron Showers," *Progress of Theoretical Physics Supplement*, vol. 6, pp. 93–155, Jan. 1958.

[14] K. Greisen, "Cosmic ray showers," *Annual Review of Nuclear Science*, vol. 10, no. 1, pp. 63–108, 1960.

[15] P. Abreu *et al.*, "The energy spectrum of cosmic rays beyond the turn-down around 10^{17} eV as measured with the surface detector of the Pierre Auger Observatory," *European Physical Journal C*, vol. 81, no. 11, p. 966, 2021. arXiv: 2109.13400 [astro-ph.HE].

[16] M. Urban, "Search for magnetically-induced patterns in cosmic ray arrival directions using a new extragalactic filter technique at the pierre auger observatory," Ph.D. dissertation, RWTH Aachen University, 2019.

[17] P. Abreu *et al.*, "Measurement of the proton-air cross section at s= 57 tev with the pierre auger observatory," *Physical review letters*, vol. 109, no. 6, p. 062 002, 2012.

[18] P. Abreu *et al.*, "Testing effects of lorentz invariance violation in the propagation of astroparticles with the pierre auger observatory," *Journal of cosmology and astroparticle physics*, vol. 2022, no. 01, p. 023, 2022.

[19] M. Unger *et al.*, "Longitudinal Shower Profile Reconstruction from Fluorescence and Cherenkov Light," Jun. 2007. arXiv: 0706.1501 [astro-ph].

[20] M. Ave, "Reconstruction accuracy of the surface detector array of the Pierre Auger Observatory," in *30th International Cosmic Ray Conference*, vol. 4, Jul. 2007, pp. 307–310. arXiv: 0709.2125 [astro-ph].

[21] J. Hersil *et al.*, "Observations of Extensive Air Showers near the Maximum of Their Longitudinal Development," *Physical Review Letters*, vol. 6, pp. 22–23, 1961.

[22] A. Aab *et al.*, "Measurement of the cosmic-ray energy spectrum above 2.5×10^{18} eV using the Pierre Auger Observatory," *Physical Review D*, vol. 102, no. 6, p. 062 005, 2020. arXiv: 2008.06486 [astro-ph.HE].

[23] M. J. Tueros, "Estimate of the Non-calorimetric Energy of Showers Observed with the Fluorescence and Surface Detectors of the Pierre Auger Observatory," in *International Cosmic Ray Conference*, ser. International Cosmic Ray Conference, vol. 33, Jan. 2013, p. 1713.

[24] V. Berezinsky, "Ultra High Energy Cosmic Ray Protons: Signatures and Observations," *Nuclear Physics B - Proceedings Supplements*, vol. 188, P. Bernardini *et al.*, Eds., pp. 227–232, 2009. arXiv: 0901.0254 [astro-ph.HE].

[25] D. Allard *et al.*, "On the transition from galactic to extragalactic cosmic-rays: Spectral and composition features from two opposite scenarios," *Astroparticle Physics*, vol. 27, no. 1, pp. 61–75, 2007, ISSN: 0927-6505.

[26] A. A. Halim *et al.*, "Constraining models for the origin of ultra-high-energy cosmic rays with a novel combined analysis of arrival directions, spectrum, and composition data measured at the pierre auger observatory," *arXiv preprint arXiv:2305.16693*, 2023.

[27] A. Aab *et al.*, "Combined fit of spectrum and composition data as measured by the pierre auger observatory," *Journal of Cosmology and Astroparticle Physics*, vol. 4, 2017.

[28] K. Greisen, "End to the cosmic ray spectrum?" *Physical Review Letters*, vol. 16, pp. 748–750, 1966.

[29] G. T. Zatsepin and V. A. Kuz'min, "Upper Limit of the Spectrum of Cosmic Rays," *Soviet Journal of Experimental and Theoretical Physics Letters*, vol. 4, p. 78, Aug. 1966.

[30] P. Abreu *et al.*, "Interpretation of the Depths of Maximum of Extensive Air Showers Measured by the Pierre Auger Observatory," *Journal of Cosmology and Astroparticle Physics*, vol. 02, p. 026, 2013. arXiv: 1301.6637 [astro-ph.HE].

[31] K. Werner *et al.*, "Parton ladder splitting and the rapidity dependence of transverse momentum spectra in deuteron-gold collisions at the bnl relativistic heavy ion collider," *Physical Review C*, vol. 74, p. 044 902, 4 Oct. 2006.

[32] F. Riehn *et al.*, "The hadronic interaction model SIBYLL 2.3c and Feynman scaling," *PoS*, vol. ICRC2017, p. 301, 2018. arXiv: 1709.07227 [hep-ph].

[33] S. Ostapchenko, "Nonlinear screening effects in high energy hadronic interactions," *Physical Review D*, vol. 74, p. 014 026, 1 Jul. 2006.

[34] A. Yushkov, "Mass Composition of Cosmic Rays with Energies above $10^{17.2}$ eV from the Hybrid Data of the Pierre Auger Observatory," *Proceeding of Science*, vol. ICRC2019, p. 482, 2019.

[35] P. Erdoğdu *et al.*, "The dipole anisotropy of the 2 Micron All-Sky Redshift Survey," *Monthly Notices of the Royal Astronomical Society*, vol. 368, no. 4, pp. 1515–1526, Apr. 2006, ISSN: 0035-8711. eprint: https://academic.oup.com/mnras/article-pdf/368/4/1515/3959229/mnras0368-1515.pdf.

[36] R. Jansson and G. R. Farrar, "A new model of the galactic magnetic field," *The Astrophysical Journal*, vol. 757, no. 1, p. 14, Aug. 2012.

[37] A. Aab *et al.*, "Cosmic-ray anisotropies in right ascension measured by the pierre auger observatory," *The Astrophysical Journal*, vol. 891, no. 2, p. 142, 2020.

[38] B. L. Welch, "The generalization of 'STUDENT'S'problem when several different population varlances are involved," *Biometrika*, vol. 34, no. 1-2, pp. 28–35, Jan. 1947, ISSN: 0006-3444. eprint: https://academic.oup.com/biomet/article-pdf/34/1-2/28/553093/34-1-2-28.pdf.

[39] H.-P. Bretz *et al.*, "Parsec: A parametrized simulation engine for ultra-high energy cosmic ray protons," *Astroparticle Physics*, vol. 54, pp. 110–117, 2014, ISSN: 0927-6505.

[40] D. Wittkowski and K.-H. Kampert, "On the anisotropy in the arrival directions of ultra-high-energy cosmic rays," *The Astrophysical Journal Letters*, vol. 854, no. 1, p. L3, 2018.

[41] R. A. Batista *et al.*, "Crpropa 3.2 — an advanced framework for high-energy particle propagation in extragalactic and galactic spaces," *Journal of Cosmology and Astroparticle Physics*, vol. 2022, no. 09, p. 035, Sep. 2022.

[42] X. Sun *et al.*, "Radio observational constraints on galactic 3d-emission models," *Astronomy & Astrophysics*, vol. 477, no. 2, pp. 573–592, 2008.

[43] R. Jansson and G. R. Farrar, "The galactic magnetic field," *The Astrophysical Journal Letters*, vol. 761, no. 1, p. L11, Nov. 2012.

[44] J. Han, "The magnetic structure of our galaxy: A review of observations," *Proceedings of the International Astronomical Union*, vol. 4, no. S259, pp. 455–466, 2008.

[45] R. Beck, "Galactic and extragalactic magnetic fields," in *AIP Conference Proceedings*, American Institute of Physics, vol. 1085, 2008, pp. 83–96.

[46] G. R. Farrar *et al.*, "The Galactic Magnetic Field and UHECR Optics," *Proceedings of Science*, vol. ICRC2015, p. 560, 2016.

[47] D. Harari *et al.*, "Signatures of galactic magnetic lensing upon ultra high energy cosmic rays," *Journal of High Energy Physics*, vol. 2000, no. 02, p. 035, 2000.

[48] M. Erdmann *et al.*, "The nuclear window to the extragalactic universe," *Astroparticle Physics*, vol. 85, pp. 54–64, 2016.

[49] K. M. Gorski *et al.*, "Healpix: A framework for high-resolution discretization and fast analysis of data distributed on the sphere," *The Astrophysical Journal*, vol. 622, no. 2, p. 759, 2005.

[50] R. A. Fisher, "Dispersion on a sphere," *Proceedings of the Royal Society of London. Series A. Mathematical and Physical Sciences*, vol. 217, no. 1130, pp. 295–305, 1953. eprint: `https://royalsocietypublishing.org/doi/pdf/10.1098/rspa.1953.0064`.

[51] W. F. G. Swann, "Application of liouville's theorem to electron orbits in the earth's magnetic field," *Physical Review*, vol. 44, pp. 224–227, 3 Aug. 1933.

[52] Rossoni, Simone and Sigl, Günter, "Crpropa high statistics simulations for uhecr anisotropy studies," *EPJ Web of Conferences*, vol. 283, p. 03 010, 2023.

[53] M. D. Domenico *et al.*, "Reinterpreting the development of extensive air showers initiated by nuclei and photons," *Journal of Cosmology and Astroparticle Physics*, vol. 2013, no. 07, p. 050, Jul. 2013.

[54] "Synchrotron radiation," in *Radiative Processes in Astrophysics*. John Wiley & Sons, Ltd, 1985, ch. 6, pp. 167–194, ISBN: 9783527618170. eprint: `https://onlinelibrary.wiley.com/doi/pdf/10.1002/9783527618170.ch6`.

[55] A. Zonca *et al.*, "Healpy: Equal area pixelization and spherical harmonics transforms for data on the sphere in python," *Journal of Open Source Software*, vol. 4, no. 35, p. 1298, Mar. 2019.

[56] J. D. Hunter, "Matplotlib: A 2d graphics environment," *Computing in Science & Engineering*, vol. 9, no. 3, pp. 90–95, 2007.

[57] C. R. Harris *et al.*, "Array programming with NumPy," *Nature*, vol. 585, no. 7825, pp. 357–362, Sep. 2020.

[58] P. Virtanen *et al.*, "SciPy 1.0: Fundamental Algorithms for Scientific Computing in Python," *Nature Methods*, vol. 17, pp. 261–272, 2020.

Acknowledgement

This work would not be possible if there were not these involving people and stuff. The author would like to express the deepest gratitude to these people:

- Dr. Rodrigo Guedes Lang. He has provided me with a lot of knowledge and support during the entire Master's thesis phase.
- Prof. Dr. Stefan Funk. He gave me the opportunity to become part of the ECAP gamma group.

The High-Performance computing (HPC) of the RRZE is very much appreciated for many parallel jobs, which accelerates the progress of this work. Simulations are made possible through `CRPropa 3.2` [41], the framework for UHECR propagation. Some of the results in this paper have been derived using the `healpy`[55] and `HEALPix`[49] package, including handling the pixelated skymaps, plotting routine, and computing the angular power spectrum. Other plots are made using `Matplotlib`[56]. Mathematical tools and numerical computations are provided by Python packages, `Numpy`[57] and `Scipy`[58].

The author is awarded the scholarship and is financially supported by the Development and Promotion of Science and Technology Talents Project (DPST), Thailand.

Statement of Authorship

I hereby confirm that this thesis is written independently without any outside help. All of the external statements are referenced from the sources listed in the bibliography and are clearly indicated in the text.

Erlangen, August 24$^{\text{th}}$, 2023.

Chaimongkol Duangchan